Charles University in Prague
Faculty of Mathematics and Physics

MASTER THESIS

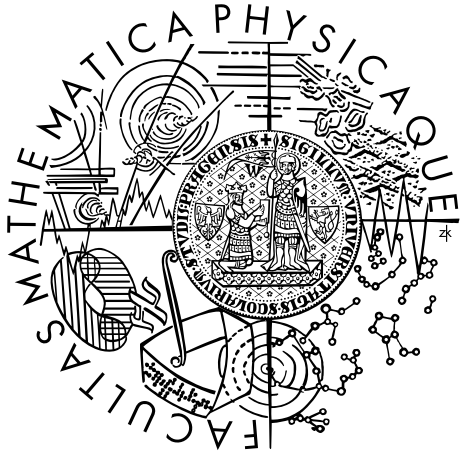

Marián Vlček

Investigation of defects in quasicrystals by positron annihilation spectroscopy

Department of Low Temperature Physics

Supervisor: doc. Mgr. Jakub Čížek, Ph.D.
Study programme: Physics
Specialization: Solid State Physics

Prague 2011

Acknowledgements

I would like to show my gratitude to my supervisor, doc. Mgr. Jakub Čížek, Ph.D., whose guidance, support and valuable advices enabled me to develop an understanding of the subject.

Marián Vlček

I hereby declare that I carried out this master thesis independently, and exclusively with the use of the cited sources, literature and other professional sources.

I understand that my work relates to rights and obligations under the Act No. 121/2000 Coll., the Copyright Act, as amended, in particular, that the Charles University in Prague has the right to conclude a license agreement for the use of this work as a school work according to Section 60 Paragraph 1 of the Copyright Act.

In Prague date 14.4.2011 Marián Vlček

Contents

Název práce: Studium defektů v kvazikrystalech metodou pozitronové anihilační spektroskopie

Autor: Marián Vlček
Katedra: Katedra fyziky nízkých teplot
Vedoucí diplomové práce: doc. Mgr. Jakub Čížek, Ph.D., Katedra fyziky nízkých teplot

Abstrakt: V predloženej práci študujeme horčíkové zliatiny obsahujúce ikosahedrálnu fázu pomocou spektroskopie doby života pozitrónov a koincidenčnej spektroskopie Dopplerovského rozšírenia anihilačného píku. Štúdiom vzorkov zliatiny WE43 modifikovanej pridaním zinku bolo zistené, že v týchto zliatinách dochádza k záchytu pozitrónov na defektoch s voľným objemom prítomných na rozhraní medzi horčíkovou matricou a ikosahedrálnou fázou $Mg_3Zn_6Y_1$. Ďalej boli študované zliatiny typu MgZnAl. V týchto zliatinách nebol pomocou spektroskopie doby života pozitrónov pozorovaný záchyt pozitrónov na defektoch s voľným objemom. Koincidenčné meranie Dopplerovského rozšírenia anihilačného píku však ukázalo, že aj v týchto zliatinách dochádza k záchytu positrónov v okolí ikosahedrálnej fázy $Mg_{44}Zn_{41}Al_{15}$. Na vysvetlenie rozdielnej podstaty záchytu pozitrónov v modifikovaných zliatinách WE43 a v zliatinách typu MgZnAl bolo navrhnutých niekoľko hypotéz.

Klíčová slova: kvázikryštály; positrónová anihilačná spektroskopia; záchyt pozitrónov; defekty s voľným objemom

Title: Investigation of defects in quasicrystals by positron annihilation spectroscopy

Author: Marián Vlček
Department:Department of Low Temperature Physics
Supervisor: doc. Mgr. Jakub Čížek, Ph.D., Department of Low Temperature Physics

Abstract: In the present work positron lifetime spectroscopy and coincidence spectroscopy of Doppler broadening of annihilation radiation were employed for investigations of defects in Mg alloys with icosahedral phase. Samples of WE43 alloy and WE43 alloy modified by addition of zinc were investigated. Positron trapping at vacancy-like defects associated with interface between the icosahedral phase $Mg_3Zn_6Y_1$ and Mg matrix was observed. Investigations of MgZnAl-based alloys were performed as well. Vacancy-like defects were not detected in MgZnAl-based alloys by positron lifetime spectroscopy. However, coincidence spectroscopy of Doppler broadening of annihilation radiation revealed that positron trapping in the vincinity of icosahedral $Mg_{44}Zn_{41}Al_{15}$ phase occurs. Several hypotheses explaining different nature of positron trapping in WE43-based and MgZnAl-based alloys were proposed.

Keywords: quasicrystals; positron annihilation spectroscopy; positron trapping; open-volume defects

1. Introduction

Quasicrystals exhibit unique structure without translation symmetry. This structure in-between crystalline and amorphous materials gives them properties such as high hardness, high corrosion and wear resistance and low surface energy. Quasicrystalline phases with icosahedral symmetry were recently observed in magnesium alloys with zinc and rare earth elements. We expect that unusual structure of quasicrystalline precipitates can lead to types of defects which do not exist in conventional magnesium alloys.

Positron annihilation spectroscopy is well-established experimental technique used for studying defects in condensed matter. Positron lifetime spectroscopy is capable of determining type and concentration of defects. Coincidence spectroscopy of Doppler broadening of annihilation radiation gives us information about chemical composition in the vincinity of defects. These two techniques together represent a powerfull tool capable of characterizing defects in given material.

In the present work positron lifetime spectroscopy and coincidence Doppler broadening were employed for investigations of defects in Mg alloys with icosahedral phase. Positron annihilation was combined with X-ray diffraction, scanning electron microscopy and microhardness measurements.

2. Physical principles of positron annihilation spectroscopy

2.1 Positron source

Radioisotopes undergoing β^+ decay are usually used as positron sources. Decay of such radioisotope can be decribed by an equation

$$ {}^{A}_{Z}X \rightarrow {}^{A}_{Z-1}X' + e^+ + \nu. \tag{2.1} $$

Nucleus ${}^{A}_{Z}X$ decays to nucleus ${}^{A}_{Z-1}X'$ with simultaneos emission of positron e^+ and neutrino ν. Typical characteristic of β^+ decay is continuous energy spectrum of kinetic energy of emitted positrons. End-point energies are usually in the range of hundreds to thousands keV. Most often used positron source is ^{22}Na. Its decay scheme is shown in figure 2.1. ^{22}Na radioisotope emits positrons with mean kinetic energy of $\sim$ 270 keV and end-point energy $E_{max} = 0.545$ MeV.

The daughter ^{22}Ne nucleus is created in excited state and de-excites by emission of γ ray with characteristic energy of 1274 keV. This γ ray is called start photon. Since lifetime of the excited ^{22}Ne level is only a few ps (see figure 2.1) the start photon appears almost simultaneously with positron and carries thereby information about time when the positron was born.

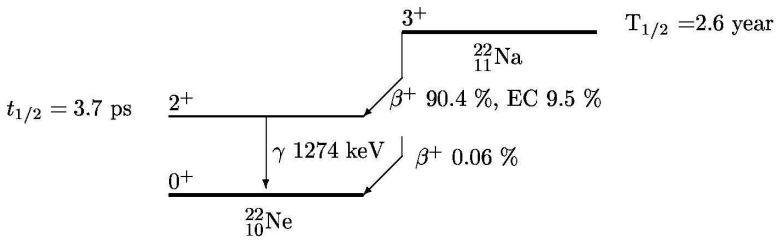

Figure 2.1: Decay scheme of the radioisotope ^{22}Na.

2.2 Thermalization of positrons

After penetrating into condensed matter positron quickly loses its initial kinetic energy and ends with energy of $\sim \frac{3}{2}kT$ (i.e. 0.039 eV at room temperature) [1].

This process is called thermalization of positrons. In the high energy region (over $\sim$ 100 eV) positrons lose their energy by excitation of core lectrons, at lower energies (100-0.1 eV) scattering by conduction electrons prevails. At lowest energies below 0.1 eV loss of energy by scattering on phonons dominates. Typical thermalization time is in order of several ps. This is roughly two orders of magnitude shorter than typical positron lifetimes in condense matter which amount to hundreds ps.

After reaching thermal equilibrium the velocity of positron is governed by classic Maxwell-Boltzmann distribution. The mean square velocity of positron is

$$v_+ \equiv \sqrt{\langle v^2 \rangle} = \sqrt{\frac{3kT}{m^*}}, \tag{2.2}$$

where k is Boltzmann constant, T temperature and m^* is the effective positron mass. The latter quantity includes contribution of phonons, positron band structure and electron-positron interaction and usually equals to $m^* \simeq 1.5m$, where m is the rest mass of positron. The mean square velocity of positron can be approximated as

$$v_+[\mathrm{nm/ps}] \simeq 5.5\sqrt{T}. \tag{2.3}$$

2.3 Positron implantation profile

The penetration depth of positrons emitted by a β^+ source with a continuous energy spectrum and the mean energy in order of hundreds kiloelectronvolts can be described by an empirical implantation profile [2]

$$P(x) = \alpha_+ e^{-\alpha_+ x}, \tag{2.4}$$

where $P(x)$ is probability that positron penetrates into depth x under surface of sample. The mean penetration depth is

$$\frac{1}{\alpha_+}[\mathrm{cm}] \simeq \frac{E_{max}[\mathrm{MeV}]}{16\varrho[\mathrm{g \cdot cm^{-3}}]}, \tag{2.5}$$

where E_{max} is the end-point energy of β^+ source and ϱ is density of sample. The mean penetration depth of positrons emited by ^{22}Na source into various metals falls into the range 10 to 500 μm. Hence, positrons probe bulk properties of the sample.

2.4 Positron states in condensed matter

After thermalization positron is scattered almost exclusively by phonons. This does not lead to a further change in the momentum distribution of thermalized positrons. In classical approximation positron performs isotropic random diffusion motion in material. Phonon scatterings leads to temperature dependence positron diffusion coefficient [3]

$$D_+ \sim \frac{1}{\sqrt{T}}. \tag{2.6}$$

Typical values of the positron diffusion coefficient at room temperature fall in the range from 0.1 to 2 $\mathrm{cm^2 s^{-1}}$. The mean free path of a thermalized positron is

$$l_+ = v_+ \tau_{ph}, \tag{2.7}$$

where τ_{ph} is the relaxation time of phonon scattering. The mean free path of positron in metals is in the order of nanometers.

The mean volume explored by a positron during its lifetime is $\lambda_+^2 L_+$, where λ_+ is positron wavelength and L_+ is the mean diffusion length of positron. The wavelength of a thermalized positron is

$$\lambda_+[\mathrm{nm}] = \frac{2\pi\hbar}{m^* v_+} \simeq 5,2\sqrt{\frac{293[\mathrm{K}]}{T[\mathrm{K}]}}. \tag{2.8}$$

The mean diffusion length L_+ expresses the mean distance which positrons travel from the point of their thermalization during their lifetime. It is defined by equation

$$L_+ = \sqrt{D_+ \tau_I}. \tag{2.9}$$

In metals the mean diffusion length is in the order of hundreds nanometers. Therefore positron explores volume containing about 10^7 atoms during its lifetime.

As positron wavelength λ_+ in condesed matter is always longer than the interatomic distance, positrons behave in condensed matter as waves. Therefore we speak about delocalized or free positrons. Annihilation rate of positron in metal is proportional to overlap of electron and positron density [4]

$$\lambda = \pi r_e^2 c \hat{n}_-, \tag{2.10}$$

where r_e is classical electron radius, c is the velocity of light and

$$\hat{n}_- = \int n_+(\boldsymbol{r}) n_-(\boldsymbol{r}) \gamma(n_-) \mathrm{d}^3\boldsymbol{r}. \tag{2.11}$$

The electron density $n_-(\mathbf{r})$ is a sum of squares of electron wavefunctions $\psi_-(\mathbf{r})$ over all occupied states $n_-(\mathbf{r}) = \sum_{e_i \leq E_F} [\psi_-(\mathbf{r})]^2$, where e_i represents energy eigenvalue of ith-level and E_F is the Fermi energy. Since there is only one positron at certain time in the sample positron density $n_+(\mathbf{r})$ is simply a square of positron wavefunction $n_+(\mathbf{r}) = [\psi_+(\mathbf{r})]^2$.

The enhancement factor γ accounts for enhancement of electron density in positron site induced by attractive Coulombic interaction. Positron in metals attracts electrons and this local enhancement of the valence electron density causes a considerable increase in the positron annihilation rate. Hence, $\hat{n}_-$ can be considered as effective electron density which affects positron. Inverse of the annihilation rate is called positron lifetime

$$\tau = \frac{1}{\lambda}. \tag{2.12}$$

Positron lifetime of deloaclized positrons in metals falls usually in range from 100 to 300 ps.

Positron is repelled by positive ions in crystal lattice. Potential which positron feels is therefore lower in open-volume defects. Typical examples are vacancies and clusters of vacancies. Energy of positron localised in open-volume defect is lower than that of delocalized one. Difference between the energy eigenvalues for these two states determines positron binding energy E_B to defect. Typical binding energies of positron trapped in vacancies are in the order of a few eV. Since local electron density in open-volume defects is lowered lifetime of trapped positrons becomes longer than lifetime of delocalized positrons.

2.5 Positron lifetime spectroscopy

As shown in equations (2.10) and (2.11) positron annihilation rate is proportional to overlap of electron and positron density. In homogenous defect free metalic material this overlap is the same for each positron, therefore all positrons annihilate with same annihilation rate. Let $n(t)$ denotes the probability that a positron at time t has not annihilated yet. As $t = 0$ we can choose the moment of implantation of positron into the material. Therefore $n(0) = 1$ and with increasing time $n(t)$ will decrease following equation

$$\frac{dn(t)}{dt} = -\lambda_B n(t), \tag{2.13}$$

where λ_B is the annihilation rate of delocalized positron in studied material. The probability $n(t)$ is therefore

$$n(t) = e^{-\lambda_B t}. \tag{2.14}$$

Positron lifetime spectrometer measures how long does it take for positron to annihilate after penetrating measured material. This means that spectrometer measures negative time derivative of $n(t)$, therefore an ideal positron lifetime spectrum S_{id} has form

$$S_{id}(t) = -\frac{dn(t)}{dt} = \lambda_B e^{-\lambda_B t}. \tag{2.15}$$

Positron lifetime $\tau_B = 1/\lambda_B$ is the expected value of this distribution. However real positron lifetime spectrometers have finite time resolution and there is also some background from random coincidences so the real spectrum can be desribed as

$$S(t) = S_{id}(t) * R(t) + B, \tag{2.16}$$

where $*$ denotes convolution, $R(t)$ is resolution function of the spectrometer and B is the background from random concidences. The resolution function $R(t)$ describes the response of spectrometer to a prompt coincidence and can be usually expressed by sum of two or three Gaussians.

In case of materials with defects the situation is more complicated. For simplicity we will consider material with one type of defect which can trap positrons. Let's denote $n_B(t)$ the probability that a positron is at time t delocalized in the material and $n_D(t)$ the probability that a positron is at time t trapped in defect. Therefore $n(t) = n_B(t) + n_D(t)$. Thermalized positron can annihilate form the delocalized state with the annihilation rate λ_B or from the trapped state at defect with the annilation rate λ_D. The probability of positron trapping in defect is given by the trapping rate K_D. There are two factors limiting positron trapping at defects: (i) positron must diffuse to the vicinity of defect, (ii) quantum transition from delocalized to localized state must occur. There are two limit cases:

1. Transition-limited regime: positron trapping rate is determined by the transition rate from delocalized to localized state. The time necessary for positron to reach vincity of defect is negligible in comparison to the time necessary for localization. The mean distance between trapping sites must be smaller than the

mean diffusion length L_+. Typical example of this case is positron trapping in monovacancies with sufficiently high concentration.

2. Diffusion-limited regime: the mean distance between defects is substantially larger than L_+. In this case positron trapping rate is limited by diffusion of positrons to the vicinity of defects. Trapping at grain boundaries or in larger precipitates are typical examples of this regime.

In general case both positron diffusion and transition rate from delocalized to localized state must be taken into account.

Positron kinetics in transition-limited regime can be described by simple trapping model (STM). Following assumptions are made in this model:

1. only thermalized positrons can be trapped
2. detrapping does not occur
3. space distribution of defects in material is uniform/

With these assumptions we obtain kinetic equations

$$\begin{aligned} \frac{dn_B(t)}{dt} &= -\lambda_B n_B(t) - K_D n_B(t) \\ \frac{dn_D(t)}{dt} &= -\lambda_D n_D(t) + K_D n_B(t). \end{aligned} \tag{2.17}$$

Initial conditions reflects the assumption that only thermalized positrons can be trapped, therefore after thermalization all positrons are in the delocalized state

$$n_B(0) = 1, \qquad n_D(0) = 0. \tag{2.18}$$

After solving the system of differential equations (2.17) we obtain the following equations

$$\begin{aligned} n_B(t) &= e^{-(\lambda_B + K_D)t} \\ n_D(t) &= \frac{K_D}{\lambda_B + K_D - \lambda_D}(e^{-\lambda_D t} - e^{-(\lambda_B + K_D)t}). \end{aligned} \tag{2.19}$$

The ideal positron lifetime time spectrum has two components in this case

$$S_{id}(t) = -\frac{d(n_B(t) + n_D(t))}{dt} = I_I \lambda_I e^{-\lambda_I t} + I_{II} \lambda_{II} e^{-\lambda_{II} t}. \tag{2.20}$$

After substitution of (2.20) into (2.19) we obtain positron lifetime τ and relative intensity I of each component

$$\begin{aligned} \tau_I &= \frac{1}{\lambda_I} = \frac{1}{\lambda_B + K_D} \\ \tau_{II} &= \frac{1}{\lambda_{II}} = \frac{1}{\lambda_D} \\ I_I &= 1 - I_{II} \\ I_{II} &= \frac{K_D}{\lambda_B + K_D - \lambda_D}. \end{aligned} \tag{2.21}$$

The trapping rate K_D is proportional to the concentration of defects c_D

$$K_D = \nu_D c_D, \tag{2.22}$$

where the constant ν_D is the specific trapping rate characteristic for each type of defects. The component with lifetime τ_{II} corresponds to positrons localized in defects and its intensity I_{II} increases with increasing concentration of defects, while the lifetime τ_{II} remains constant. On the other hand, the lifetime τ_I corresponding to the free positron component decreases with increasing concentration of defects.

If $K_D \gg \lambda_B$ then the lifetime τ_I and the intensity I_I of the first component become essentially zero and so called saturated positron trapping occurs. In this case we get one component spectrum with lifetime τ_D and it is not possible to determine the concentration of defects. The applicability of the simple trapping model can be checked by the following formula

$$\lambda_B = I_I \lambda_I + I_{II} \lambda_{II}. \tag{2.23}$$

If this equation does not hold then simple trapping model cannot be used because its assumptions are not fulfilled.

2.6 Coincidence Doppler broadening of positron annihilation radiation

During annihilation of electron-positron pair momentum and energy must be conserved, therefore at least two annihilation photons must be created. Since three and more photon events are much less probable than the two photon annihilation they will be not discussed further.

The kinetic energy of thermalized positron in condensed matter is negligible compared to the kinetic energy of surrounding electrons. Momentum of electron-positron pair is therefore determined by the momentum of electron which annihilated positron. Non-zero momentum of annihilating electron-positron pair in the laboratory frame leads to Doppler shift ΔE in energy of annihilation photons

$$\Delta E = \frac{1}{2} c p_L, \tag{2.24}$$

where p_L is the momentum component of the pair in the direction of emitted photon. Doppler shift causes broadening of the annihilation peak located at 511 keV. Shape of the annihilation peak consequently reflects one-dimensional distribution of electron momentum component into the connecting the source and detector. Since each chemical element has a unique momentum distribution of core electrons Doppler broadening of positron annihilation radiation can reveal chemical composition of sites where positrons annihilate.

In coincidence Doppler broadening spectroscopy (CDB) energy of both antiparallel annihilation photons are measured by two detectors. Only coincidence events, i.e. such events where annihilation photon was detected at the same time in both detectors are recorded. Coincidence measurement drastically reduces

background (typically by three orders of magnitude). This enables to resolve contribution of rare events where positrons are annihilated by high momentum core electrons.

Central part of the annihilation peak corresponds to annihilation with low-momentum conduction electrons. Momentum of core electrons is higher and therefore annihilations with them contribute to the tails of the annihilation peak. Electron density at open-volume defect is generally lowered, the density of core electron is lowered more than the density of conduction electrons. Therefore with increasing fraction of positrons trapped in defects annihilation peak becomes narrower.

Shape of the annihilation peak can be described by parameters S and W. The S parameter is defined as relative area of the central part of the peak. The W parameter is on the other hand defined as relative area of the peak tails. Magnitude of the S parameter is proportional to the fraction of positrons annihilating with conduction electrons whereas the W parameter describes the fraction of positrons annihilating with core electrons.

Boundaries of areas used for calculation of S and W parameters are usually chosen to maximize observed variation of parameters. The area corresponding to the S parameter generally contains one half of total peak area. The area corresponding to the W parameter should be chosen to contain predominantly contribution of core electrons. Absolute values of both parameters do not have any significance because they depend on the choice of area boundaries, meaningful are only their relative changes. In general with increasing concentration of defects the S parameter increases, while the W parameter decreases.

Another possibility of expressing changes of the annihilation peak shape is to use ratio curve. This curve is constructed by dividing the spectrum of annihilation peak of measured material by that of reference material. Doppler broadening of annihilation peak is symetric therefore only one half of ratio curve is usually shown.

2.7 Quasicrystals

Translation symmetry imposes constraints on possible orders of symmetry axes in periodically ordered crystall lattices. Elementary units with 2,3,4 and 6-fold rotational symmetries preserve translation symmetry and fill space without creating gaps or overlaps. However in 1984 X-ray diffractograms exhibiting icosahedral five-fold symmetry axis were observed by Shechtman et al. in rapidly cooled Al-Mn alloy [5].

It can be proved that rotation about 5-fold symmetry axis or any axis with symmetry higher than 6-fold fail to transform lattice into itself [6]. Hence such symmetry axes are forbidden in crystals. However aperiodic tiling of space exhibiting these 'forbidden' symmetries can be created if multiple elementary units are used. One of such tiling is Penrose tiling of two-dimensional plane formed by rombuses of two types. Thin rombus has vertex with angle of 36°, thick rombus has vertex angle of 72°. Penrose tiling lacks any translational symmetry and exhibits both reflection symmetry and fivefold rotational symmetry, as shown in figure 2.2. The ratio of the number of thick to thin rombuses is equal to the

golden ratio $\varphi = \frac{1+\sqrt{5}}{2}$, therefore it is impossible to define finite unit cell with the same ratio of the number of thick to thin rombuses as the ratio for the infinite tiling. Three dimensional analog of Penrose tiling can be constructed using five units shown in figure 2.3 [7].

Another way of structure description of quasicrystals is the projection method [8]. Fow simplicity we will consider one-dimensional quasicrystal. Let's consider square lattice with the lattice parameter a and with a coordinate system X_1 and X_2 turned by the angle $\theta = \arctan(\tau^{-1})$ with respect to axes of the second coordinate system $X_\parallel$ and $X_\perp$. The axis $X_\parallel$ is called physical or parallel space and axis $X_\perp$ is called additional or perpendicular space. Let's define so called projection tube, a strip of width $l = a(\cos\theta + \sin\theta)$ parallel to $X_\parallel$. Positions of lattice sites in one-dimensional quasicrystal are then determined by projection of the square lattice sites inside the projection tube onto the physical space $X_\parallel$.

There are two kinds of distances between lattice sites of such quasicrystals: long distances $L = a\cos\theta$ and short distances $S = a\sin\theta$. The sequence of long and short distances follows the Fibonacci sequence. This technique can be extended to higher dimensions, three-dimensional (3D) quasicrystals can be descibed by using 3D physical space and 3D additional space, i.e. by projection of a periodical lattice in a 6D space into 3D space.

Excitations of the quasicrystal lattice can be described by projection technique [8]. Quasicrystal density can be written in the form

$$\rho(\mathbf{r}_\parallel) = \int \rho(\mathbf{r}) n(\mathbf{r}_\perp) d^3\mathbf{r}_\perp, \tag{2.25}$$

where $\rho(\mathbf{r})$ is density of six dimensional hypercrystal, $n(\mathbf{r}_\perp)$ represents projection tube. Density in the physical space can be expanded in the Fourier series:

$$\rho(\mathbf{r}_\parallel) = \sum_Q \rho_Q \exp(i\mathbf{Q}\mathbf{r}), \tag{2.26}$$

where $\mathbf{Q}$ are vectors of the reciprocal lattice of a six-dimensional hypercrystal. Distortions of $\rho(\mathbf{r})$ are visible as additional phases $F_Q(\mathbf{r})$ in equation (2.26). These distortions be expanded into components of parallel and perpendicular spaces

$$F_Q(\mathbf{r}) = \mathbf{Q}_\parallel \mathbf{u}(\mathbf{r}) + \mathbf{Q}_\perp \mathbf{w}(\mathbf{r}), \tag{2.27}$$

where vectors fields $\mathbf{u}(\mathbf{r})$ and $\mathbf{w}(\mathbf{r})$ describe phonons and phasons respectively. Phasons are responsible for local configurations in physical space that are forbidden in the perfect two-fragment model. Phasons are physically realized by atomic displacements, which may involve numerous individual atom jumps. This becames possible due to additional degrees of freedom used in projection formalism.

Plastic deformation is dependent on dislocation mobility. However, in quasicrystals the Burgers dislocation vector contains always a phason component, therefore mobility of dislocations in quasicrystals is limited by diffusion. Due to this reason dislocation mobility is very low for temperatures under 600 °C.

Quasicrystalline aperiodic structure is preserved on clean surfaces of quasicrystals. Surface of quasicrystals has low energy, approximately 25% higher than in teflon. This is caused by presence of pseudogap in the electronic spectrum [8].

Most of discovered quasicrystalline materials were prepared as single phase materials [9] [10] [11]. However recently quasicrystalline precipitates in Mg-Zn-RE alloys were observed [12]. We expect that unique structure of these precipitates could lead to improvement of mechanical properties of magnesium alloys.

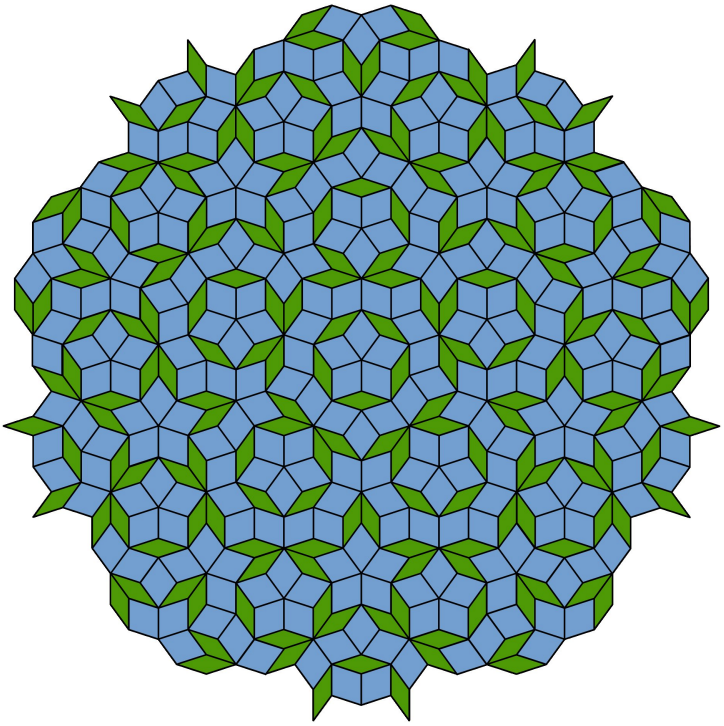

Figure 2.2: Penrose tiling [13].

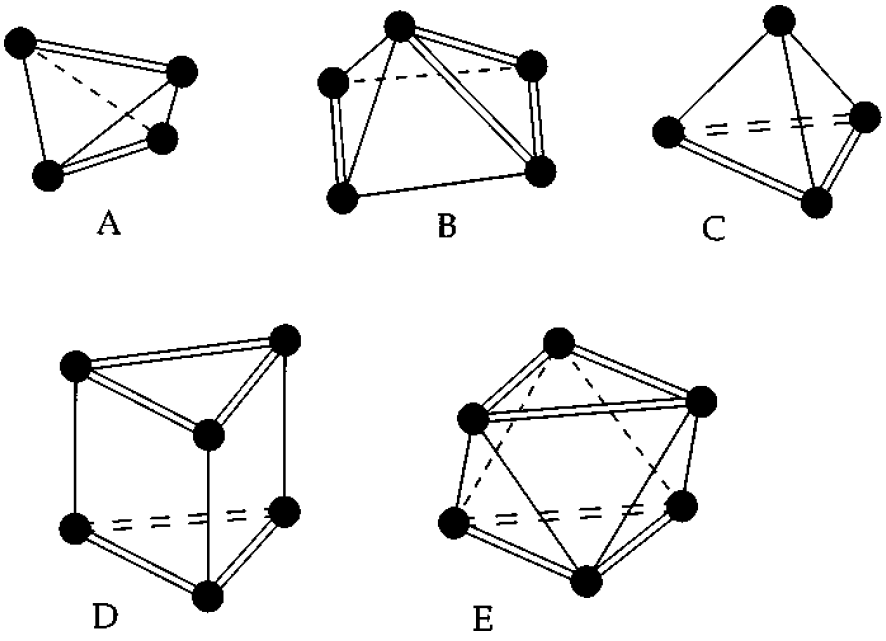

Figure 2.3: Canonical units of 3D icosahedral tiling [7].

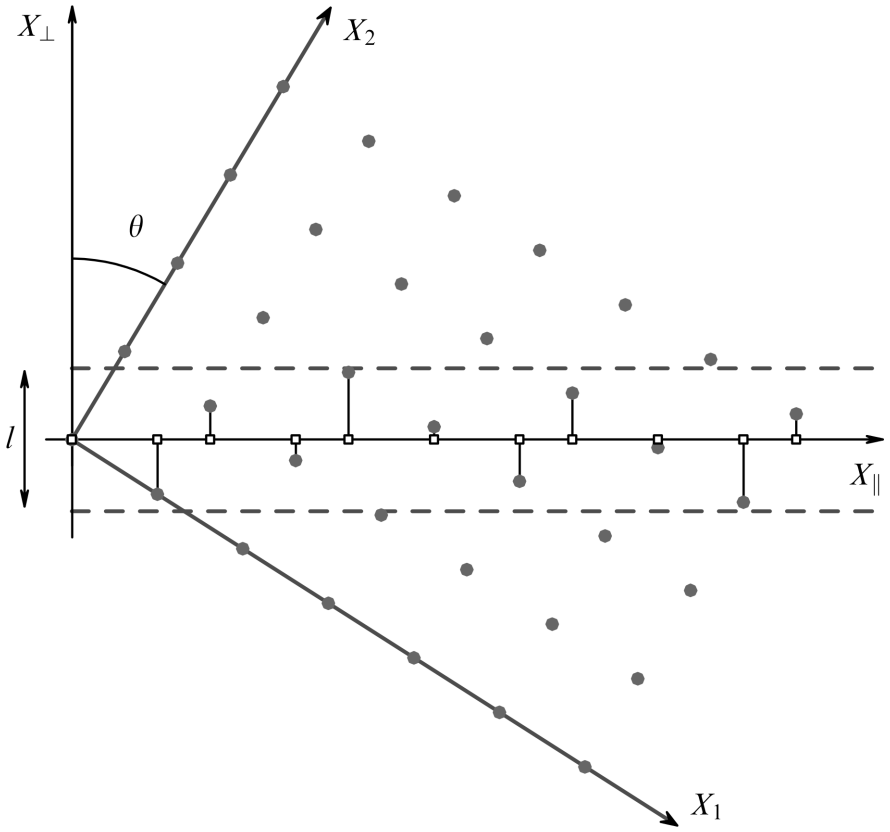

Figure 2.4: Construction of one-dimensional quasicrystal by the projection method. θ - angle between two coordinate systems $X_\parallel$, $X_\perp$ and X_1, X_1; l - width of the projection tube [8].

3. Experimental techniques

3.1 Hardness measurements

Measurements of mechanical properties represent important complement to microstructural methods. The Vickers indentation hardness test has several advantages compared to tensile tests and also to some other hardness tests, such as Brinell test. In the first place it is virtually nondestructive method because indentations are very small compared to indentation after Brinell test. Hence, it is possible to test small samples repeatedly. This property of Vickers hardness test enables us to measure hardness after each isochronal annealing step.

Hardness measurements gives us valuable information about precipitation hardening in the studied material. The Vickers test has very wide scale and can be used for any metal. The unit of hardness determined by the test is known as Vickers Pyramid number (HV).

Diamond tip in shape of square-based pyramid with angle of opposing faces of 136° is used as indenter in Vickers hardness test. Length of diagonals of indentation d_1 and d_2 are measured after the test. Hardness number HV is determined as ratio of force F applied to the indenter in kilogram-force (kgf) and area A of resulting indentation in mm^2

$$HV = \frac{F}{A}. \tag{3.1}$$

Area A is calculated from expression

$$A = \frac{d^2}{2\sin(136°/2)}, \tag{3.2}$$

where d is the arithmetic mean of diagonals d_1 and d_2. Hence,

$$HV = \frac{2F\sin(136°/2)}{d^2} \approx \frac{1.8544F}{d^2}, \tag{3.3}$$

where F is given in kgf and d in mm. In SI units, kgf must be converted to newtons by multiplying by standard gravity $g_0 = 9.80665$ ms^{-2}, i.e. 1 kfg = 9.80665 N.

When HV is expressed in SI units, yield strength of non-work-hardening material can be approximated as [14]

$$\sigma_y = \frac{HV}{3}. \tag{3.4}$$

Vickers hardness numbers are reported in form $x\mathrm{HV}l/t$, where x is the hardness number, HV denotes Vickers hardness scale, l indicates the load used in kgf and t is the loading time. If the loading time t falls into the range from 10 to 15 s, it is usually not written expicitly. Distance between indentation should be more than 2.5 times indentation diameter to avoid work-hardened regions of neighbouring indentations. Vickers hardness was measured on polished samples using microhardness tester Struers Duramin 300. Each measurement was repeated at least ten times to improve accuracy of measurement and estimate variance of measured hardness.

3.2 Scanning electron microscopy

Scanning electrom microscopy (SEM) images were taken by FEI Phenom microscope. This microscope has a detector of backscattered electrons. Backscattered electrons are high-energy electrons from primary beam that were scattered back from specimen by elastic scattering. Since scattering cross-section increases with increasing atomic number, heavier elements are represented by lighter areas on resulting image than lighter elements. Hence, SEM images exhibit so called Z-contrast. This can be demonstrated on image of MgZn alloys shown in figure 4.3. Zinc has higher atomic number (30) than magnesium (12), therefore areas with higher zinc content are lighter than zinc poor regions.

Furthermore volume fraction of eutectic was determined using following procedure. Greyscale images were converted to binary black-and-white scale. Threshold level of this conversion was carefully adjusted to produce accurate results. Finally relative fraction of white areas in the image corresponds to volume fraction of zinc-rich regions. Multiple images of the same alloy were processed to improve accuracy of measurement and estimate variance of volume fraction.

3.3 X-ray diffraction

X-ray diffraction is powerful experimental technique capable of determining phase composition and lattice parameters of phases present in the studied material. X-ray diffraction spectra were measured in symmetrical Bragg-Brentano geometry on Panalytical X'Pert PRO MRD diffractometer. Measured spectra were fitted by psedo-Voigt profile function to obtain accurate positions θ of the peaks. Interplanar distances d_{hkl} of crystallographic planes with Miller indices (hkl) and positions of peaks area are connected by Bragg's law

$$n\lambda = 2d_{hkl}\sin\theta, \tag{3.5}$$

where λ is the wavelength of X-rays and n is the order of diffraction. Therefore interplanar distance d_{hkl} for the first order diffraction used in our case can be calculated according to the formula:

$$d_{hkl} = \frac{\lambda}{2\sin\theta}. \tag{3.6}$$

3.4 Positron lifetime spectroscopy

A $^{22}Na_2CO_3$ activity of 1.5 MBq deposited on a 2μm Mylar foil was used as positron source for positron lifetime spectroscopy. Scheme of digital positron lifetime (LT) spectrometer is shown in figure 3.1. Detailed description of spectrometer is given in [15] and [16]. Scintillation detectors made of BaF_2 crystalls are attached to photomultipliers (PMT) Hamatsu H3378. Anode signal from PMTs is passively splitted. One part is connected directly to a pair of fast 8-bit digitizers Acqiris DC211 with sampling rate of 4 GHz. Second part is connected

to concidence circuit. Signal is firstly amplified by fast amplifier HP MSA-0204 and then inverted by inverting transformer (IT) Ortec IT 100. The output of the IT is connected to the constant fraction differential disciminator (CFDD) Ortec 583. CFDD produces logic pulse at the moment when the pulse on the input of the CFDD reaches given fraction of its own height. Hence, timing information on the output of CFDD is independent of the pulse height. Outputs of CFDDs are passively summed and connected to external trigger input of the digitizer. Trigger level of the master digitizer is set so that only sum of logic pulses from both CFDDs may fire trigger. Digitized waveforms are transferred to computer and stored on external hard-drive. Subsequently LT spectrum is constructed by offline analysis of sampled waveforms by specialized software routine [17]. Resulting LT spectrum is then fitted by the method of least squares. Example of fitted LT spectrum is shown in figure 3.2.

Since some positrons annihilate inside the positron source, real LT spectrum contains inevitable a contribution of positrons annihilated in the source. In this work the source contribution was detemined by measurement of reference well-annealed Mg sample exhibiting a simgle component spectrum with lifetime of 225 ps. In our case, there are two source components: shorter component with lifetime of 368 ps and intensity of 8% and longer component with lifetime 1.8 ns and intensity 1%. The former component represents a contribution of positrons annihilated in the $^{22}Na_2CO_3$ source spot and the latter component can be attributed to ortho-positronium formed in covering Mylar foils.

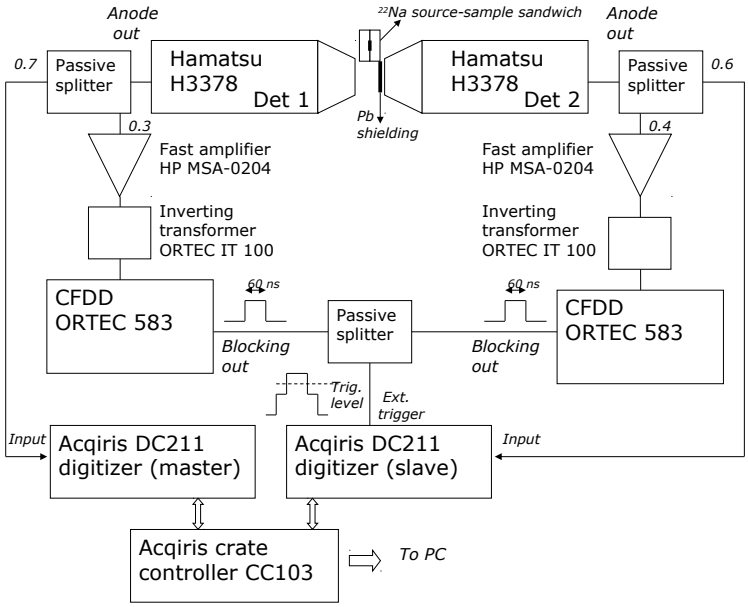

Figure 3.1: Scheme of digital positron lifetime spectrometer.

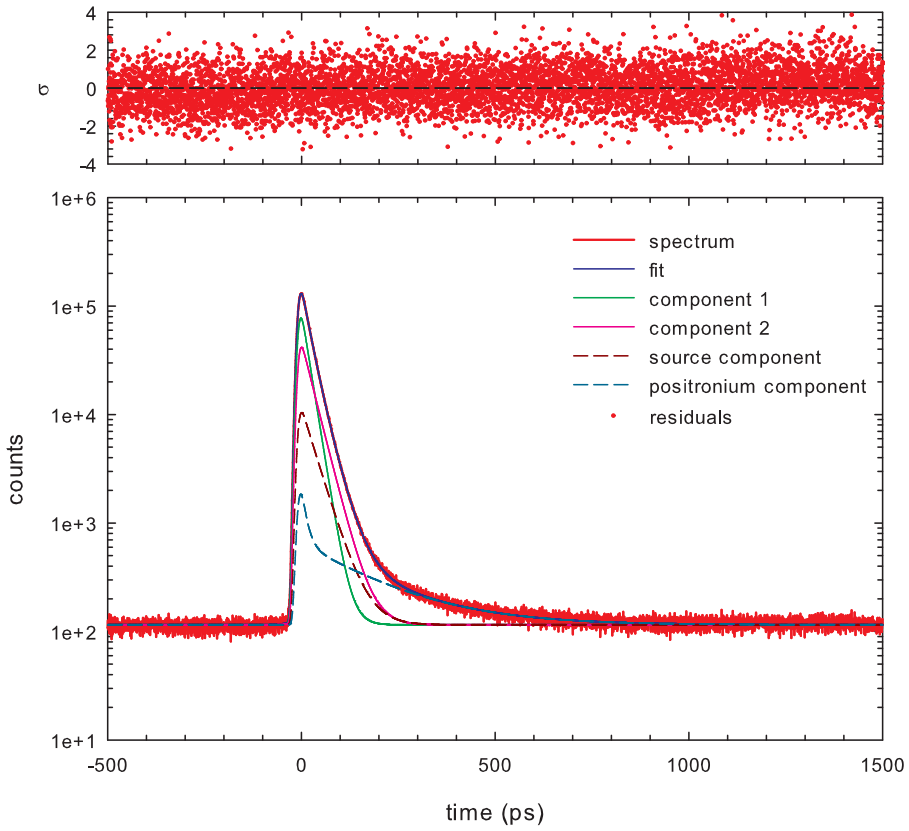

Figure 3.2: Fitted LT spectrum of WE43 alloy modified by addition of 26 wt.% of Zn (WE43+26Zn).

3.5 Coincidence Doppler-broadening spectroscopy

Scheme of coincidence spectrometer for measurement of Doppler broadening of annihilation radiation is shown in figure 3.3. High-purity germanium (HPGe) detectors, Ortec GEM35190 and GEM35P, are used because of their excelent energy resolution. The energy of the detected photon is proportional to the height of the signal on the output of the detector. Signals from the detectors are amplified and shaped by spectroscopic amplifiers (SA). Pseudo-gaussian shaping with time constant of 4 μs is used. Output pulses from spectroscopic amplifiers are lead to analog-to-digital converters (ADC) Canberra 8713 which are conected to computer.

Signals from HPGe detectors are also analyzed in the coincidence circuit, which guarantees that only events when both detectors detect simultaneously gamma ray are recorded. This circuit consists of constant fraction discriminators (CFD) and time-amplitude converter (TAC) combined with single channel analyzer (SCA). CFD produces logic pulse at the moment when the pulse on the input of the CFD reaches given fraction of its own height. Hence, timing information on the output of CFD is independent on the pulse height if pulse shape is preserved. The output signal of one CFD is connected to the start input of the TAC. The output signal of the second CFD is delayed by approximately 250 ns

and connected to the stop input of the TAC. The amplitude of the signal produced by TAC is proportional to the time between start and stop signals. TAC produces logical pulse only if signal falls into predetermined time-window. Signal from TAC is connected to the gate inputs of ADCs. Digitized values are sent to the computer only when logical signal indicating coincidence event is present at the gate input of the ADCs.

Two-dimensional (2D) coincidence Doppler broadening (CDB) spectrum, i.e. the sum of energies E_1 and E_2 measured by the first and the second detector, respectively, are plotted versus the difference of these energies. 2D CDB spectrum of well-annealed magnesium is shown in figure 3.4. Sum of energies E_1 and E_2 is

$$E_1 + E_2 - 2m_e c^2 = -E_B, \tag{3.7}$$

where m_e is electron rest mass, c is speed of light and E_B is binding energy of annihilated electron. However due to finite energy resolution of the spectrometer, resolution function is observed in the real spectrum instead of delta peak at energy $-E_B$ in the ideal case.

Doppler shift ΔE from equation (2.24) can be determined by substracting E_2 from E_1

$$E_1 - E_2 = 2\Delta E = cp_L, \tag{3.8}$$

where p_L is the momentum component of the annihilating pair into the direction of emitted photon. Therefore, cutting of 2D CDB spectrum along the line $E_1 = E_2$ gets us the resolution function of CDB spectrometer. The cut along the line $E_1 + E_2 - 2m_e c^2 = 0$ results in profile of Doppler broadened annihilation peak. Cuts of the 2D CDB spectrum shown in figure 3.4 are plotted in figure 3.5.

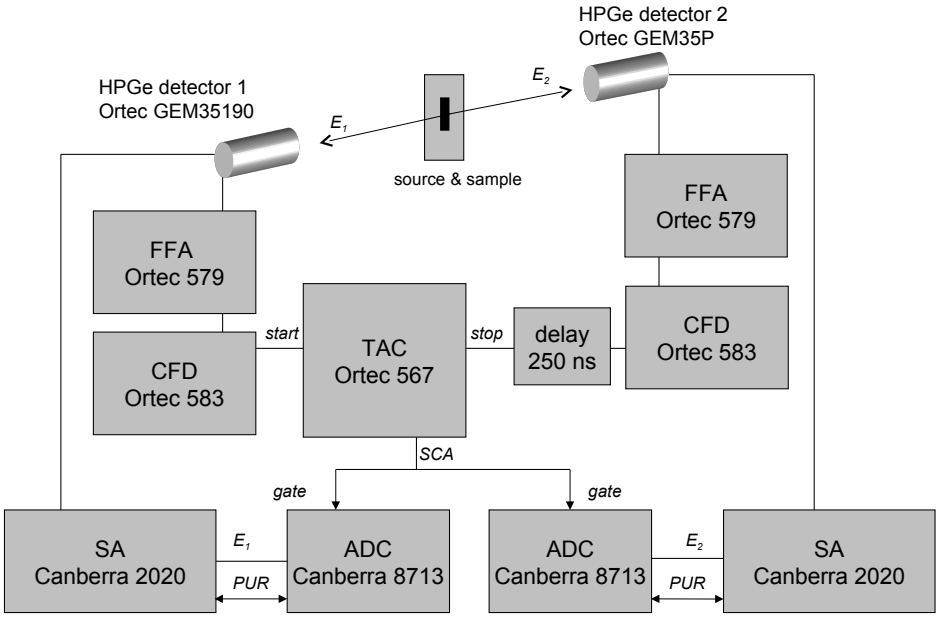

Figure 3.3: Scheme of CDB spectrometer.

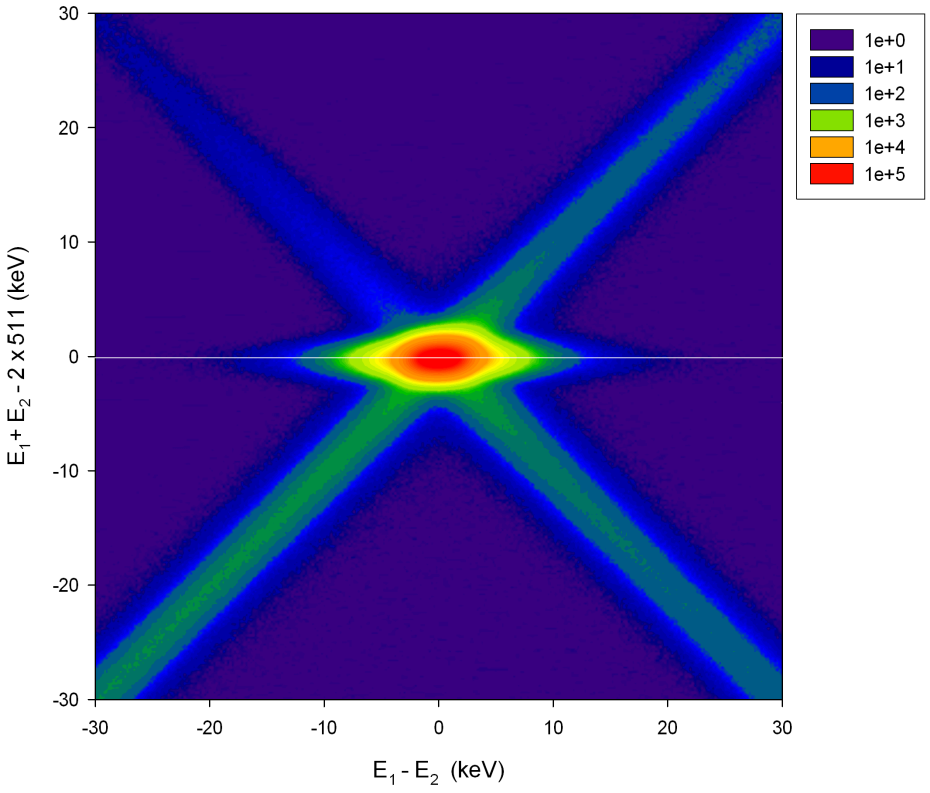

Figure 3.4: Two-dimensional CDB spectrum of magnesium, total statistics in the spectrum is 91 millions events.

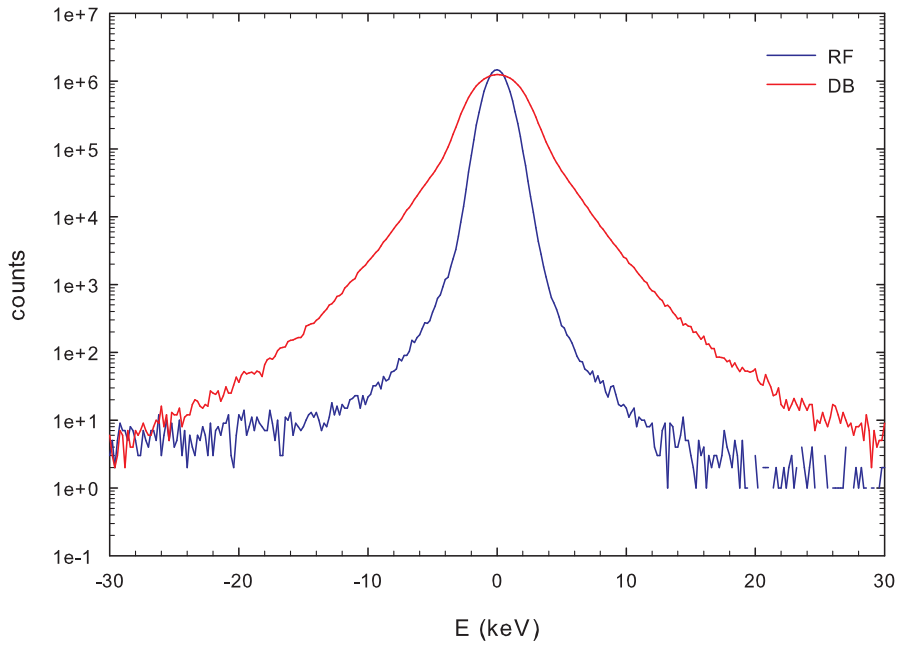

Figure 3.5: Cuts of 2D CDB spectrum of magnesium: RF - resolution function, DB - Doppler broadened annihilation profile

4. Results

4.1 Model binary alloy Mg6Zn

4.1.1 Samples

Samples of binary alloy Mg6Zn with composition Mg 93.8 wt.%, Zn 6.2 wt.% (Mg 97.7 at.%, Zn 2.3 at.%) were prepared by squeeze casting. The concentration of zinc in the samples is near the solubility limit of zinc in magnesium [18]. Phase diagram of Mg-Zn system is shown in figure 4.1. As-cast samples were subjected to isochronal annealing with steps 20 °C / 20 min. Each annealing step was finished by quenching into water of room temperature.

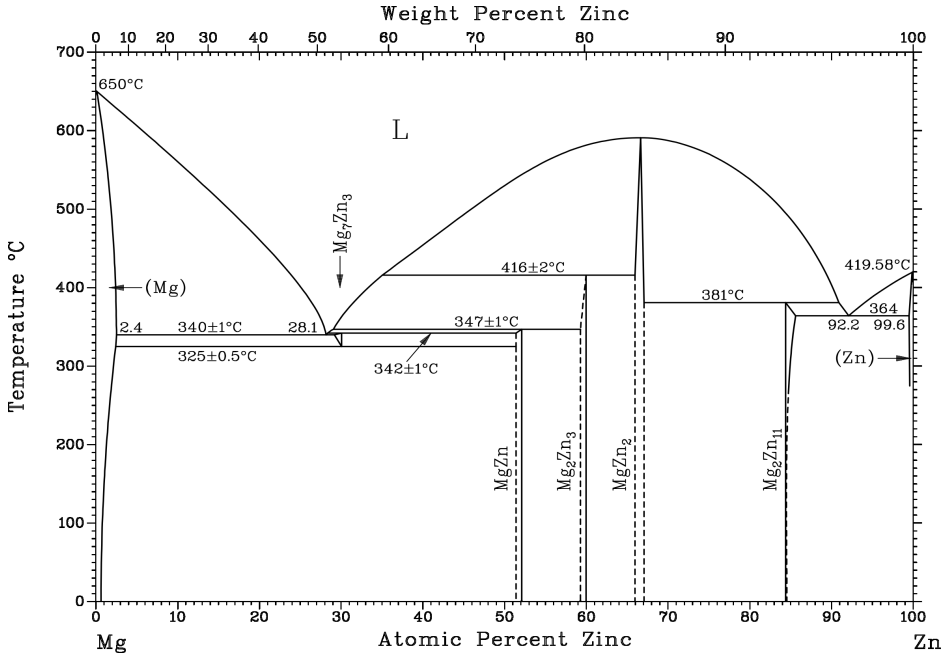

Figure 4.1: Phase diagram of Mg-Zn system [19] [20] [21] [22].

4.1.2 Mechanical properties and phase composition

Vickers hardness test was done after each annealing step. Results are shown in the figure 4.2. Hardness of the samples decreases during annealing up to 200 °C most probably due to recovery of dislocations introduced into the sample by cutting and shaping. At 220 °C sudden increase in hardness ocurs. This is due to precipitation of small precipitates that harden the sample. The equilibrium phase diagram in figure 4.1 shows that Zn solubility in Mg reaches maximum of 6.2 wt.% (2.4 at.%) at temperature 340 °C. This concentration corresponds approximately to Zn content in the Mg6Zn alloy studied in this work. At lower temperatures Zn solubility in Mg decreases.

Hence, from the figure 4.1 one can deduce that particles which cause hardening at 220 °C could be precipitates of MgZn phase. However, because of enhanced Zn concentration around grain boundaries detected by SEM, see the next paragraph, one cannot exclude also precipitation of Mg_2Zn_3 phase with higher Zn content. At higher temperatures precipitates grow and became too coarse to cause precipitation hardening and at even higher temperatures they finally dissolve. Small peak centered around 390 °C is statistically insignificant and was not observed using other methods.

Scanning electron microscopy image (Z-contrast) of the as-cast sample is shown in the figure 4.3. We can see some randomly distributed bright particles corresponding most probably to undissolved Zn. Moreover, one can recognize diffuse areas with higher zinc content around grain boundaries. Black spots and lines are artifacts caused by polishing of sample surface.

Figure 4.4 shows SEM image of Mg6Zn sample annealed at 300 °C for 100 min. Enhanced Zn concentration along grain boundaries is still visible but in comparison with the as-cast sample the contrast is significantly lower and grain interiors become brighter in the annealed sample. This indicates gradual dissolution of Zn in Mg matrix. This process further continues during annealing at higher temperatures. SEM image of the sample annealed at 500 °C for 30 min shown in figure 4.5 exhibits almost uniform contrast and no enhancement of Zn content at grain boundaries is visible anymore.

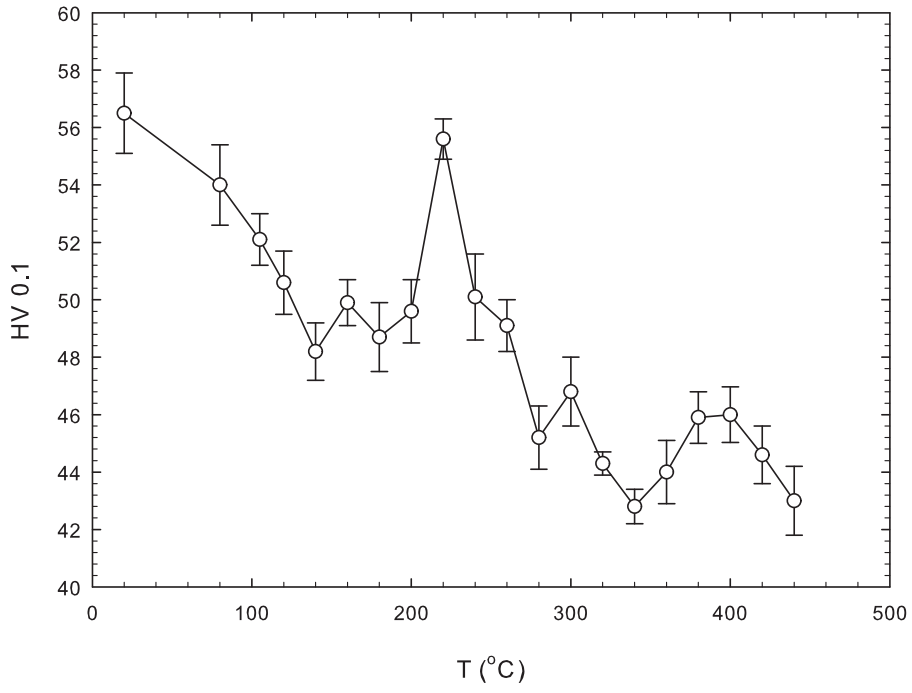

Figure 4.2: Dependence of hardness on temperature of isochronal annealing for Mg6Zn sample.

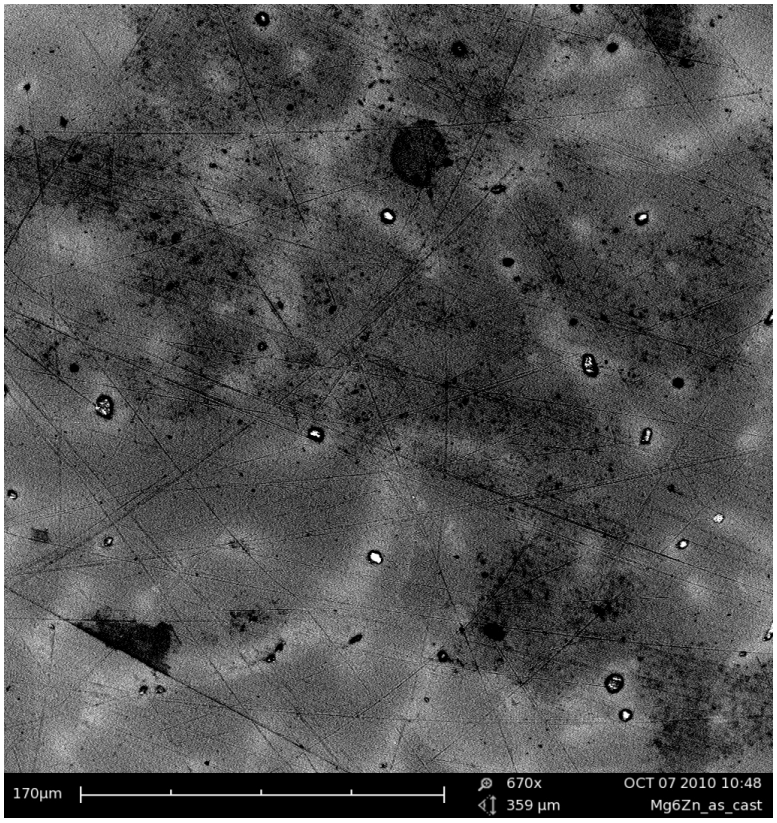

Figure 4.3: SEM image of as-cast Mg6Zn alloy.

Figure 4.4: SEM image of Mg6Zn alloy annealed at 300 °C for 100 min.

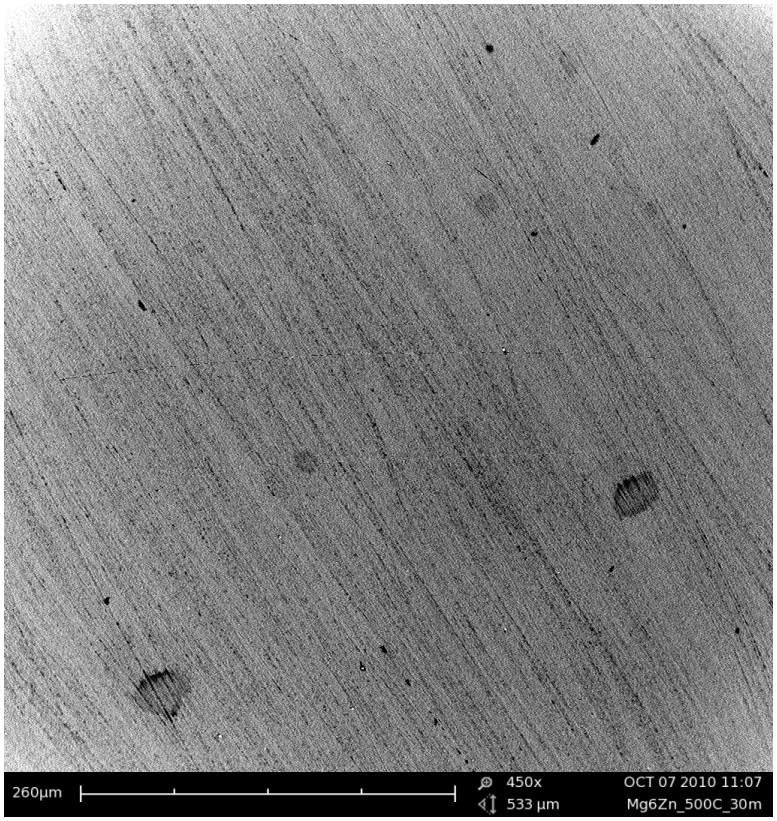

Figure 4.5: SEM image of Mg6Zn alloy annealed at 500 °C for 30 min.

4.1.3 Defect studies

Positron lifetime (LT) investigations were performed on the as-cast sample and subsequently on the sample subjected to isochronal annealing after each annealing step. Results of LT investigations are shown in figures 4.6 and 4.7. Lifetime spectra except of those measured on the sample annealed at 220 and 240 °C exhibit a single component with lifetime τ_1 which agrees well with the bulk magnesium positron lifetime of $\sim$ 225 ps [23].

In the temperature range from 220 to 240 °C LT spectra consist of two components. The lifetime τ_1 of the first component is shortened due to positron trapping in defects. Second component with lifetime $\tau_2 \sim 255$ ps represents a contribution of positrons trapped at defects. Obviously these defects were introduced by formation of Zn-rich precipitates (probably MgZn or Mg_2Zn_3 phase) which causes hardening. Lattice mismatch between the precipitates and Mg matrix is compensated by vacancy-like open-volume defects. Relative intensity I_2 of the second component is plotted in figure 4.7 and reaches maximum at 220 °C.

Results of LT measurements were analyzed by application of STM. Summary of this analysis is shown in table 4.1. The lifetime τ_B was determined using equation (2.23) to check applicability of STM in this case. Calculated values of τ_B are in good agreement with the bulk positron lifetime of well-annealed magnesium 225 ps. This testifies that assumptions of STM are fulfilled and STM can be used to estimate concentration of defects in Mg6Zn alloy.

Positron trapping rate K_D to vacancy-like misfit defects and precipitate-

matrix interfaces was calculated from equation (2.21). Concentration of misfit defects c_D was determined using equation (2.22). The positron specific trapping rate ν_D to vacancies in metals usually falls into the range $10^{14} - 10^{15}$ s^{-1} [24]. The value $\nu_D = 10^{14}$ s^{-1} was used to estimate the concentration of vacancy-like misfit defects in Mg6Zn alloy. There are two valid reasons why we chose ν_D value corresponding to the lower limit of the aforementioned range of specific positron trapping rates for vacancies in metals:

(i) because of relatively low density of valence electrons in the interatomic regions in magnesium lattice the positron binding energy to vacancy in magnesium is lower than in dense metals. Therefore, the specific positron trapping rate to vacancy in magnesium is expected to be lower than in metals with higher electron density in the lattice.

(ii) the open volume of misfit defect is a little bit smaller than open volume of vacancy in Mg matrix. This is reflected also by shorter lifetime of positrons trapped at misfit defect. Hence, misfit defect can be considered as squeezed vacancy and slight reduction of free volume reduces also the cross section for positron trapping.

One can see in table 4.1 that highest concentration of vacancy-like defects was detected in the sample annealed at 220 °C. Note that this temperature corresponds also to the maximum hardening, see figure 4.7.

	τ_1 (ps)	I_1 (%)	τ_2 (ps)	I_2 (%)	τ_B (ps)	K_D (10^8s^{-1})	c_D
Mg6Zn - 220 °C	218(1)	83(2)	256 Fix	18(2)	224(5)	1.21(1)	$1.21(1)\times10^{-6}$
Mg6Zn - 240 °C	220(2)	92(5)	256 Fix	8(5)	223(5)	0.48(5)	$4.8(5)\times10^{-7}$

Table 4.1: Results of LT measurements of Mg6Zn alloy.

CDB measurements were performed on the Mg6Zn sample subjected to isochronal annealing. Ratio curves of Mg6Zn alloy annealed at various temperatures are shown in figure 4.8.

In the high momentum range where the contribution of positrons annihilated by core electrons dominates the ratio curve ρ measured on Mg6Zn alloy can be expressed as linear combination

$$\rho = (1 - F_D)(\xi_{Mg,B} + \xi_{Zn,B}\rho_{Zn,B}) + F_D(\xi_{Mg,D}\rho_{Mg,D} + \xi_{Zn,D}\rho_{Zn,D}), \qquad (4.1)$$

where F_D is the fraction of positrons trapped in defects, $\rho_{Zn,B}$ is the the ratio curve of free positrons annihilated by Zn electrons, $\rho_{Mg,D}$ and $\rho_{Zn,D}$ denotes the ratio curve for positrons trapped at defects and annihilated by Mg and Zn electrons, respectively. The coefficients $\xi_{Mg,B}$ and $\xi_{Zn,B}$ normalized so that $\xi_{Mg,B} + \xi_{Zn,B} = 1$ denote the fraction of free positrons annihilated by Mg and Zn electrons, respectively. The coefficients $\xi_{Mg,D}$ and $\xi_{Zn,D}$ which again fulfill the normalization condition $\xi_{Mg,D} + \xi_{Zn,D} = 1$, represent the fraction of positrons trapped at defects and annihilated by Mg and Zn electrons, respectively.

The ratio curves $\rho_{Zn,B}$ $\rho_{Mg,D}$ and $\rho_{Zn,D}$ were determined by measuring reference samples of well-annealed and cold rolled pure Mg and Zn samples. In well-annealed samples all positrons annihilate from the free state. Hence, the momentum distribution measured on well-annealed Mg sample was used as reference spectrum, i.e. all ratio curves are related to this sample and the CDB ratio curve measured on well-annealed pure Zn equals $\rho_{Zn,B}$.

Plastic deformation introduces dislocations and also vacancies into cold rolled samples. Dislocation line itself is too shallow trap to confine positron [25], but certain fraction F_D of positrons in cold rolled reference samples annihilates from the trapped state at vacancies anchored in the compressive elastic field around dislocations. The CDB ratio curve (related to well-annealed Mg) for cold rolled Mg can be expressed as

$$\rho = (1 - F_D) + F_D \rho_{Mg,D}. \tag{4.2}$$

The ratio curve $\rho_{Mg,D}$ was determined from equation 4.2 using the fraction F_D obtained from positron lifetime measurement of cold rolled Mg sample. The ratio curve (related to pure well-annealed Mg) measured on cold rolled Zn can be expressed as

$$\rho = (1 - F_D)\rho_{Zn,B} + F_D \rho_{Zn,D}. \tag{4.3}$$

The ratio curve $\rho_{Zn,D}$ was determined from equation 4.3 using the fraction F_D obtained from positron lifetime measurement of cold rolled Zn sample. The reference ratio curve $\rho_{Mg,D}$ is plotted in figure 4.9, while the ratio curves $\rho_{Zn,B}$ and $\rho_{Zn,D}$ are plotted in figure 4.10.

Samples annealed at 220 and 240 °C exhibit a peak in the ratio curves at $8{\times}10^{-3}$ m_0c representing a contribution of positrons trapped at open-volume defects, cf. figure 4.9.

Since presence of this peak in CDB spectra coincides with the appearence of a defect domponent in LT spectra and maximum hardening, it is clear that it represents contribution of positrons trapped at misfit defects associated with Zn-rich precipitates. This peak is also present at 200 and 280 °C but it is not so pronounced.

While in the low-momentum region the shape of CDB ratio curves resembles that of deformed magnesium, in the high momentum region measured ratio curves substantially differs from that of deformed magnesium. Values of ratio curve for deformed magnesium are less than one while values of all measured ratio curves approximately equal to one in the high momentum region.

This discrepancy can be resolved by combining ratio curves of deformed magnesium and zinc. The ratio curves of zinc exhibit a broad peak in the high momentum region that compensates low values of ratio curve of deformed magnesium.

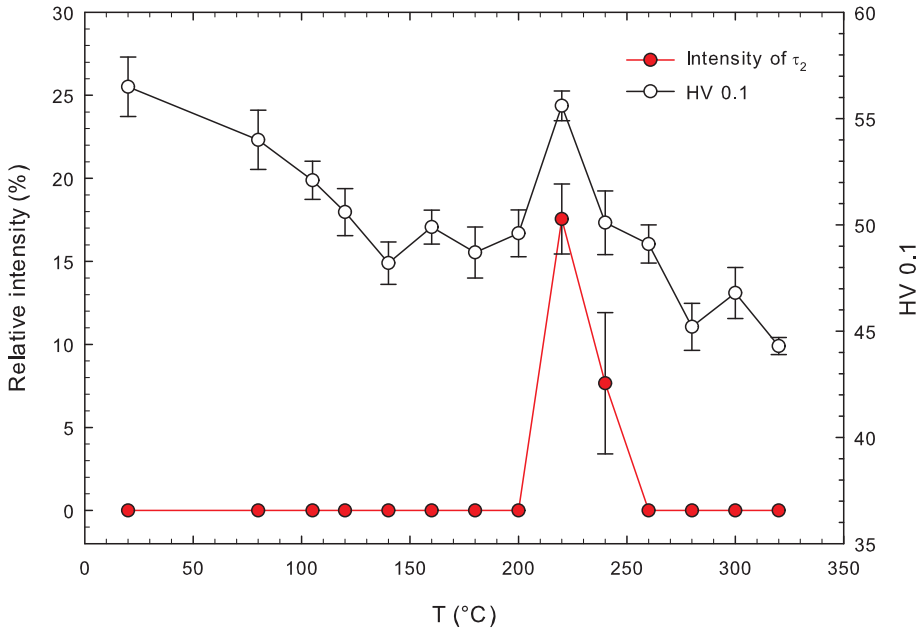

Figure 4.6: Temperature dependence of positron lifetimes τ_1 and τ_2 of the components resolved in positron lifetime spectra of Mg6Zn.

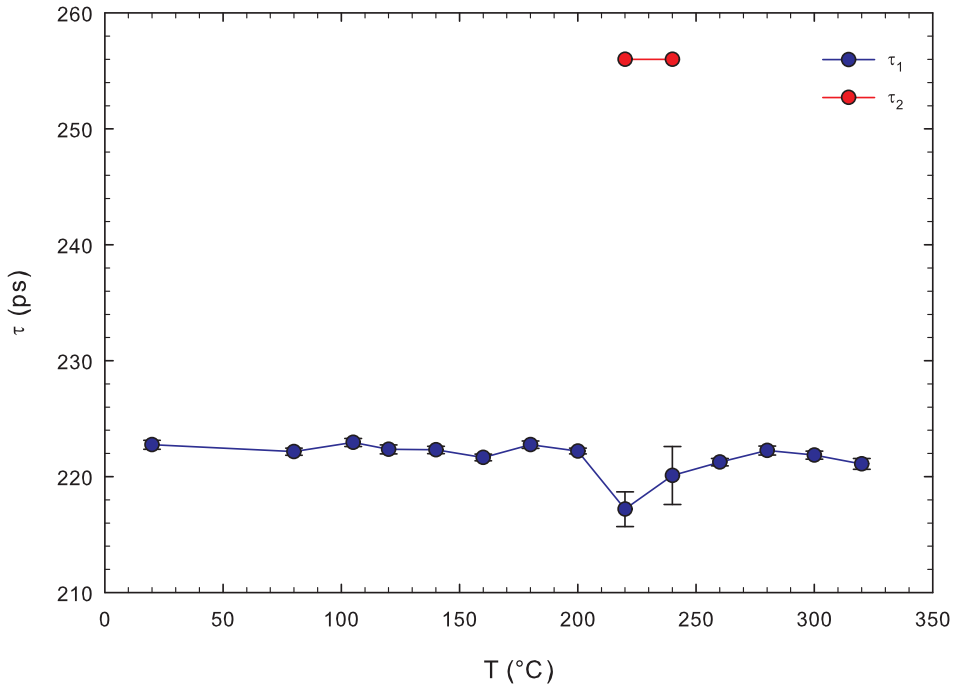

Figure 4.7: Red full circles - Temperature dependence of the relative intensity I_2 of the component originating from positrons trapped at defects in Mg6Zn. Open circles - temperature dependence of microhardness.

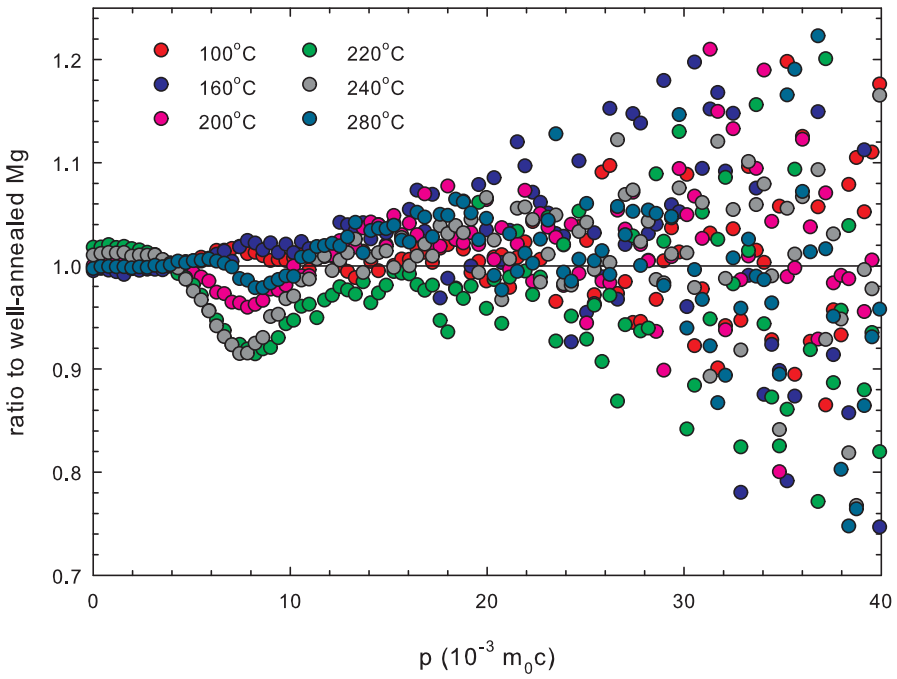

Figure 4.8: CDB ratio spectra (related to well annealed Mg) of Mg6Zn annealed at various temperatures.

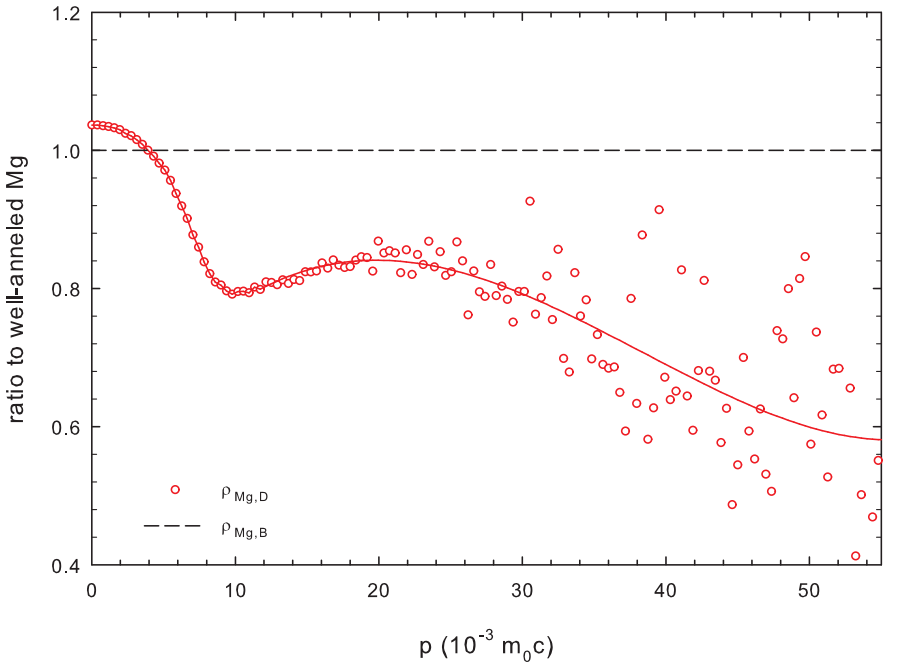

Figure 4.9: Reference ratio curves (related to well-annealed Mg) for ratio curves of free positrons annihilated by Mg electrons $\rho_{Mg,B}$ and positrons trapped at defects and annihilated by Mg electrons $\rho_{Mg,D}$.

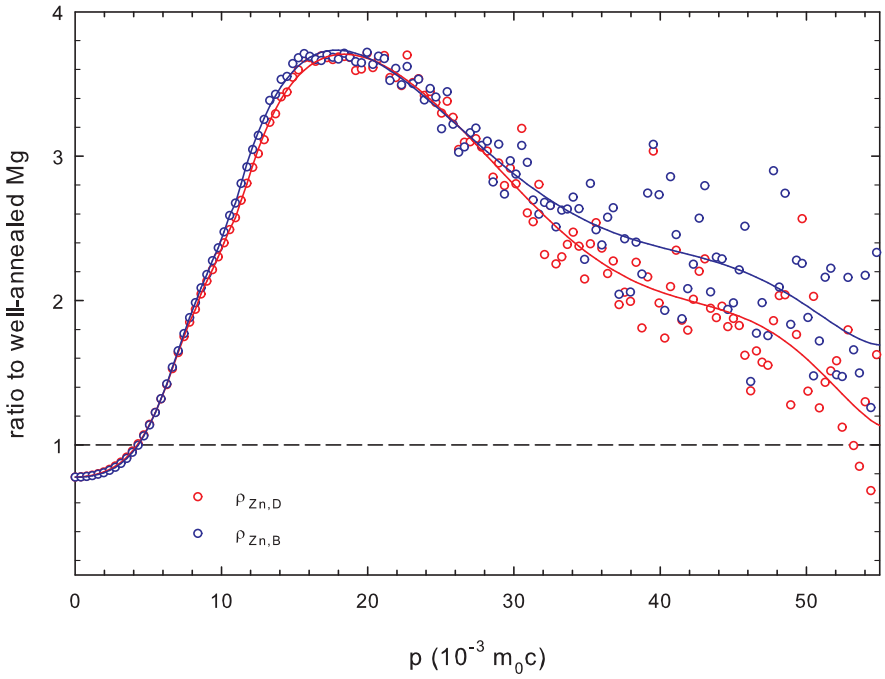

Figure 4.10: Reference ratio curves (related to well-annealed Mg) for ratio curves of free positrons annihilated by Zn electrons $\rho_{Zn,B}$ and positrons trapped at defects and annihilated by Zn electrons $\rho_{Zn,D}$.

4.2 WE43-based alloys

4.2.1 Samples

Samples of WE43 (Mg-Y-Nd-Zr based alloy) and WE 43 modified by addition of 14 wt.% (WE43+14Zn) and 26 wt.% (WE43+26Zn) of Zn were investigated. Their compositions were determined by chemical analysis and are shown in table 4.2 in wt.% and in table 4.3 in at.%.

	Zn	Y	Nd	Zr	Gd	Mg
WE43	-	2.95	2.48	0.30	0.15	balance
WE43+14Zn	13.8	3.06	1.04	0.29	0.1	balance
WE43+26Zn	25.82	3.02	1.16	0.27	0.17	balance

Table 4.2: Chemical composition in wt.% of the WE43-based alloys.

	Zn	Y	Nd	Zr	Gd	Mg
WE43	-	0.84	0.44	0.08	0.02	balance
WE43+14Zn	5.83	0.95	0.20	0.09	0.02	balance
WE43+26Zn	11.95	1.03	0.24	0.09	0.03	balance

Table 4.3: Chemical composition in at.% of the WE43-based alloys.

4.2.2 Mechanical properties and phase composition

Vickers hardness tests were done for each sample and measured values are shown in table 4.4. The hardness of samples increases with increasing zinc content in alloys. SEM images of samples are shown in figures 4.12 to 4.14. Eutectic is preferentially formed at grain boundaries. Volume fractions of eutectic determined from SEM images are shown in table 4.5.

WE43 sample has the lowest volume fraction of eutectic and diffuse contrast along grain boudaries can bee seen in SEM images. In WE43 sample areas with higher zinc content exist around grain boundaries and eutectic does not exhibit lamellar structure present in WE43+14Zn and WE43+26Zn samples. Lamellar structure of the eutectic in WE43+26Zn alloy can be clearly seen in figure 4.15.

It is also evident that volume fraction of the eutectic increases with increasing zinc content of alloys. WE43-based alloys are hardened by the eutectic phase. This is also demonstrated by hardness measurements of the matrix and the eutectic shown in the table 4.4. When HV0.1 test with the load of 0.1 kgf is used, indentations are large enough to cover the matrix and the eutectic at the same time. However when HV0.025 test with load of 25 gf is used, it is possible to measure the matrix and the eutectic almost separately.

Optical micrographs of indentations obtained by optical microscopy are shown in figure 4.11. It is clear that dimensions of indentation into eutectic (figure 4.11 B) are significantly smaller than size of indention into Mg matrix (figure 4.11 A). This demonstrates that eutectic is substantially harder than Mg matrix which is testified also by HV values in table 4.4.

	WE43	WE43+14Zn	WE43+26Zn
HV0.1	87 ± 2	94 ± 2	125 ± 4
HV0.025 - Matrix	-	101 ± 5	120 ± 2
HV0.025 - Eutectic	-	157 ± 6	195 ± 10

Table 4.4: Comparision of hardness of the matrix and the eutectic

	WE43	WE43+14Zn	WE43+26Zn
vol. frac. of eutectic (%)	1.8 ± 0.1	9.8 ± 0.7	25.1 ± 0.8

Table 4.5: Volume fraction of the eutectic in WE43-based alloys

Phase compositions of samples was determined by XRD measurements. Diffractograms of the studied samples are shown in figures 4.16 to 4.17. Following phases except magnesium matrix were identified: tetragonal phase $Mg_{41}Nd_5$; face-centered cubic (FCC) Mg_7Zn_3 phase; FCC $Mg_3Zn_3Y_2$ W-phase; FCC $Mg_5Nd_{0.4}Y_{0.6}$ β_1-phase and icosahedral phase $Mg_3Zn_6Y_1$.

Peaks corresponding to each identified phase were fitted by pseudo-Voigt function and lattice parameters were calculated. Results are shown in table 4.6. Interplanar distances of icosahedral $Mg_3Zn_6Y_1$ phase calculated from XRD spectra were compared to interplanar distances obtained from selected area electron diffraction (SAED) [26]. Comparison of results is shown in table 4.7. Interplanar distances obtained by XRD and SAED are in good agreement.

Phase composition of Mg-Zn-Y system is dependent on ratio of zinc to yttrium (Zn/Y) content in wt.% [27]. At high Zn/Y ratios (∼10) close to binary Mg-Zn system Mg_7Zn_3 phase is formed. Medium Zn/Y ratios (5–7) favors the formation of icosahedral phase $Mg_3Zn_6Y_1$. In the region of low Zn/Y ratios (below 1.5–2.5) $Mg_3Zn_3Y_2$ phase is formed.

	WE43	WE43+14Zn	WE43+26Zn
Zn/Y ratio	0	4.5	8.5
Mg_7Zn_3 - fcc	-	-	a = 14.107(9) Å
$Mg_3Zn_3Y_2$ - fcc	-	a = 6.854(5) Å	-
$Mg_5Nd_{0.4}Y_{0.6}$ - fcc	a = 7.487(5) Å	-	-
$Mg_{41}Nd_5$ - tetragonal	a = 14.87(3) Å	-	-
	c = 10.14(2) Å	-	-

Table 4.6: Lattice parameters of identified phases and Zn/Y ratio of WE43-based alloys.

	WE43+14Zn XRD (Å)	WE43+14Zn SAED (Å)	WE43+26Zn XRD (Å)	WE43+26Zn SAED (Å)
i1a	6.495(8)	-	6.49(2)	-
i1b	6.14(2)	6.18(9)	6.063(9)	6.1(2)
??	-	3.82(3)	-	3.74(7)
i2a	3.389(2)		3.384(2)	-
i2b	3.272(5)	3.30(8)	3.277(5)	3.20(6)
i3a	2.34848(3)	2.36(2)	2.3556(4)	-
i3b	-	-	2.34160(5)	2.32(2)
i4	2.2780(3)	-	2.2899(4)	-
i5	2.1503(8)	-	2.1501(4)	-
i6a	2.06911(3)	2.03(2)	2.0769(3)	-
i6b	-	-	2.0640(5)	-
i7a	1.9986(3)	1.91(3)	2.01(5)	-
i7b	-	-	1.9863(7)	1.96(3)
i8a	1.7956(3)	-	1.8134(7)	-
i8b	1.7735(7)	-	1.7740(8)	-
i9a	1.45115(4)	1.48(1)	1.45045(8)	-
i9b	-	-	1.4457(7)	1.43(1)
i10	-	-	1.415(1)	-
i11	1.2793(3)	1.26(1)	1.2762(3)	-
i12	1.10(1)	-	1.1028(1)	-
i13	0.9398(1)	-	0.94005(7)	-

Table 4.7: Comparison of interplanar distances measured by XRD and SAED in the icosahedral phase $Mg_3Zn_6Y_1$ in WE43-based alloys.

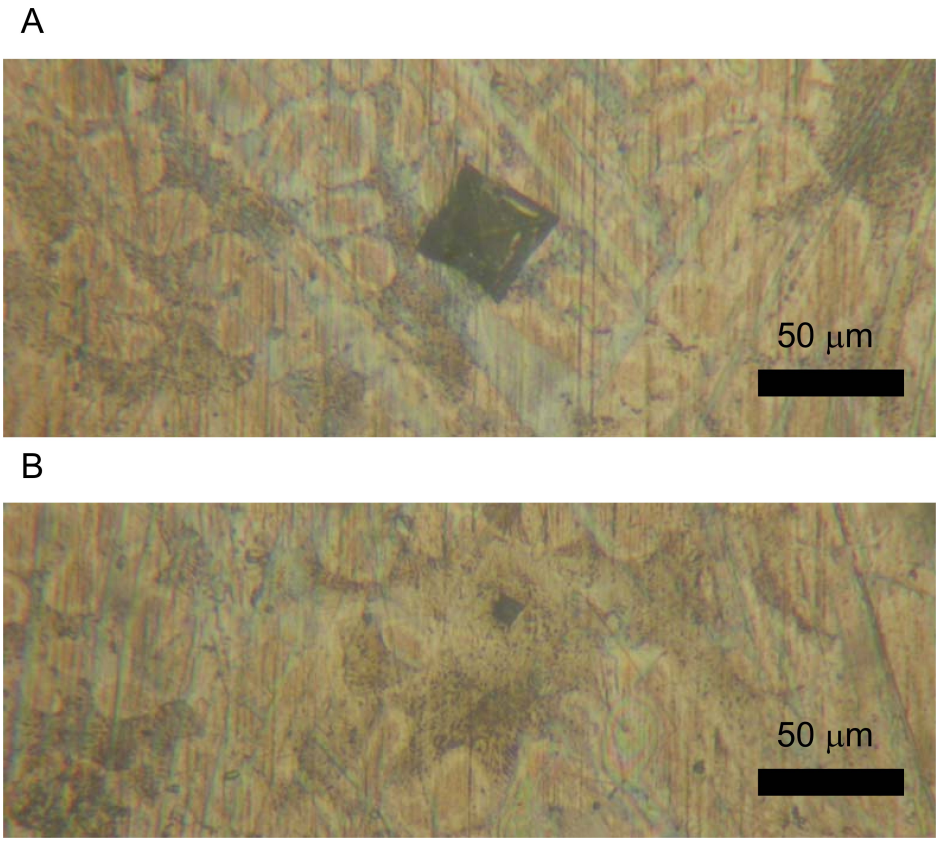

Figure 4.11: Comparision of indentations after HV0.025 hardness test of WE43+26Zn alloy: A - matrix, B - eutectic.

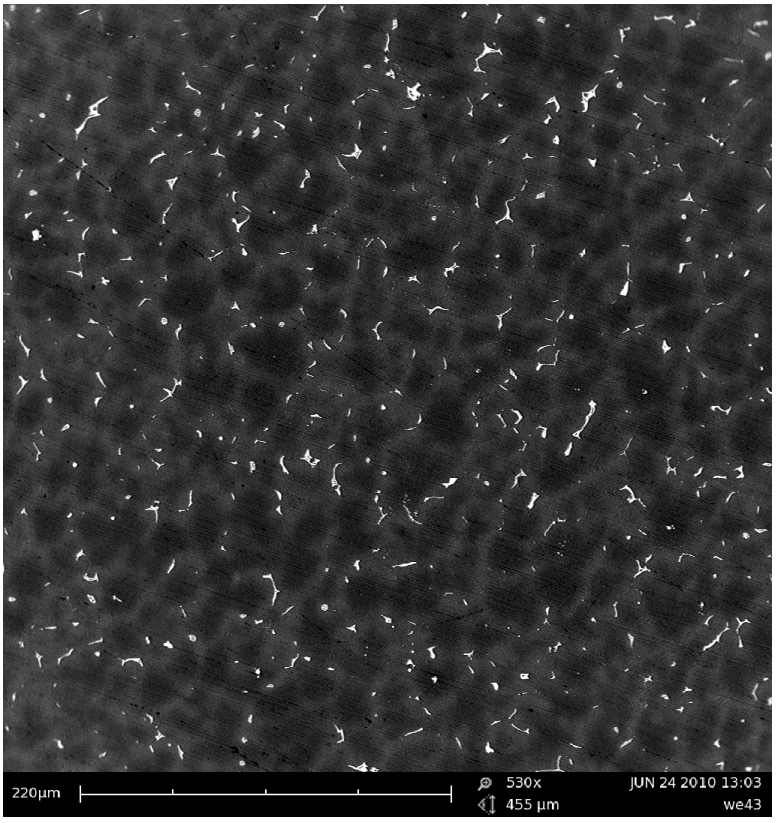

Figure 4.12: SEM image of as-cast WE43 alloy.

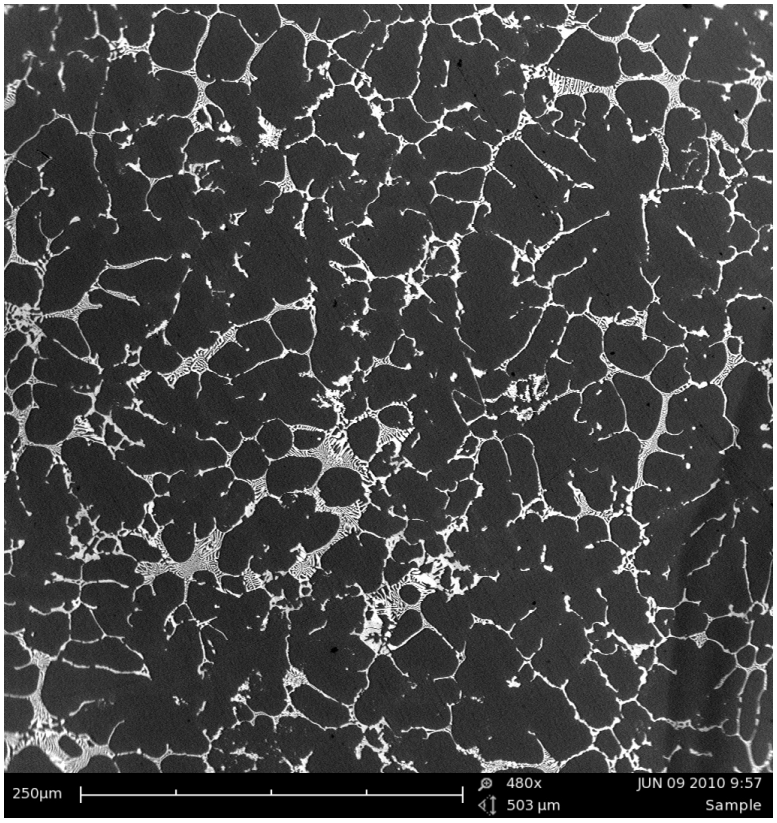

Figure 4.13: SEM image of as-cast WE43+14Zn alloy.

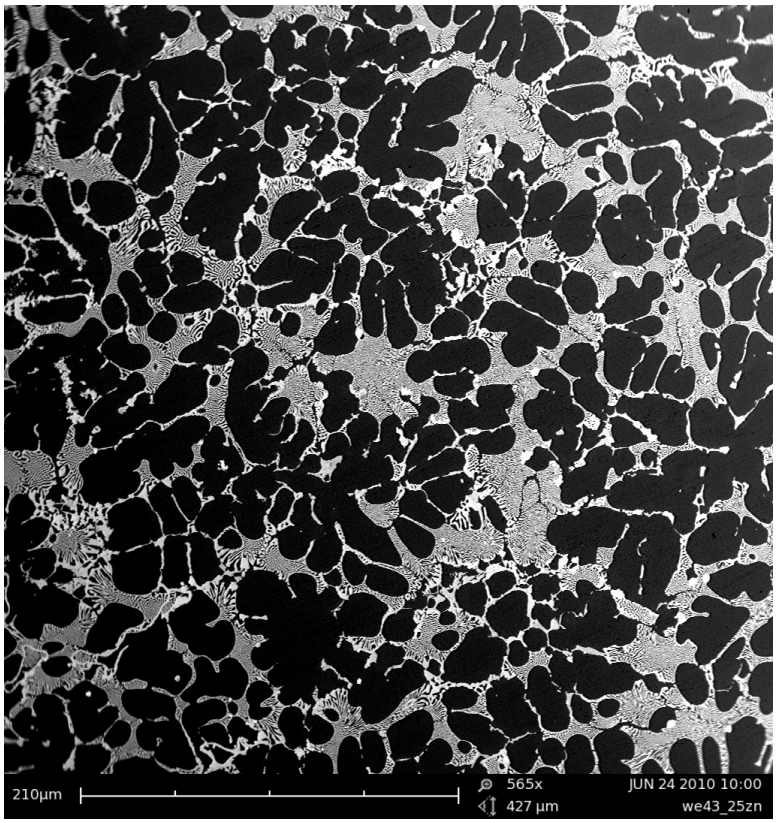

Figure 4.14: SEM image of as-cast WE43+26Zn alloy.

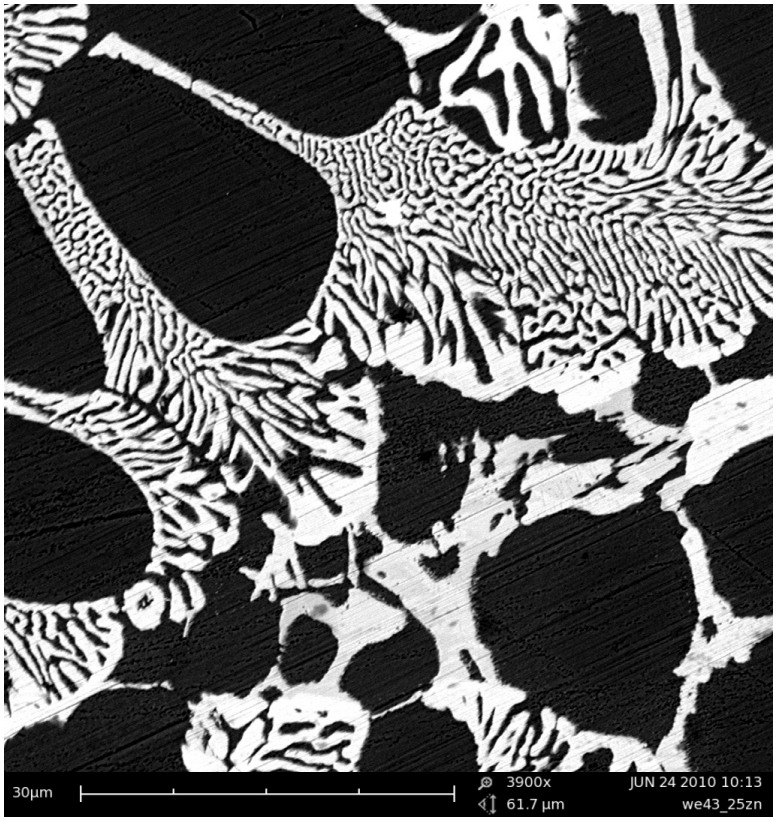

Figure 4.15: SEM image of as-cast WE43+26Zn, detail of the eutectic phase.

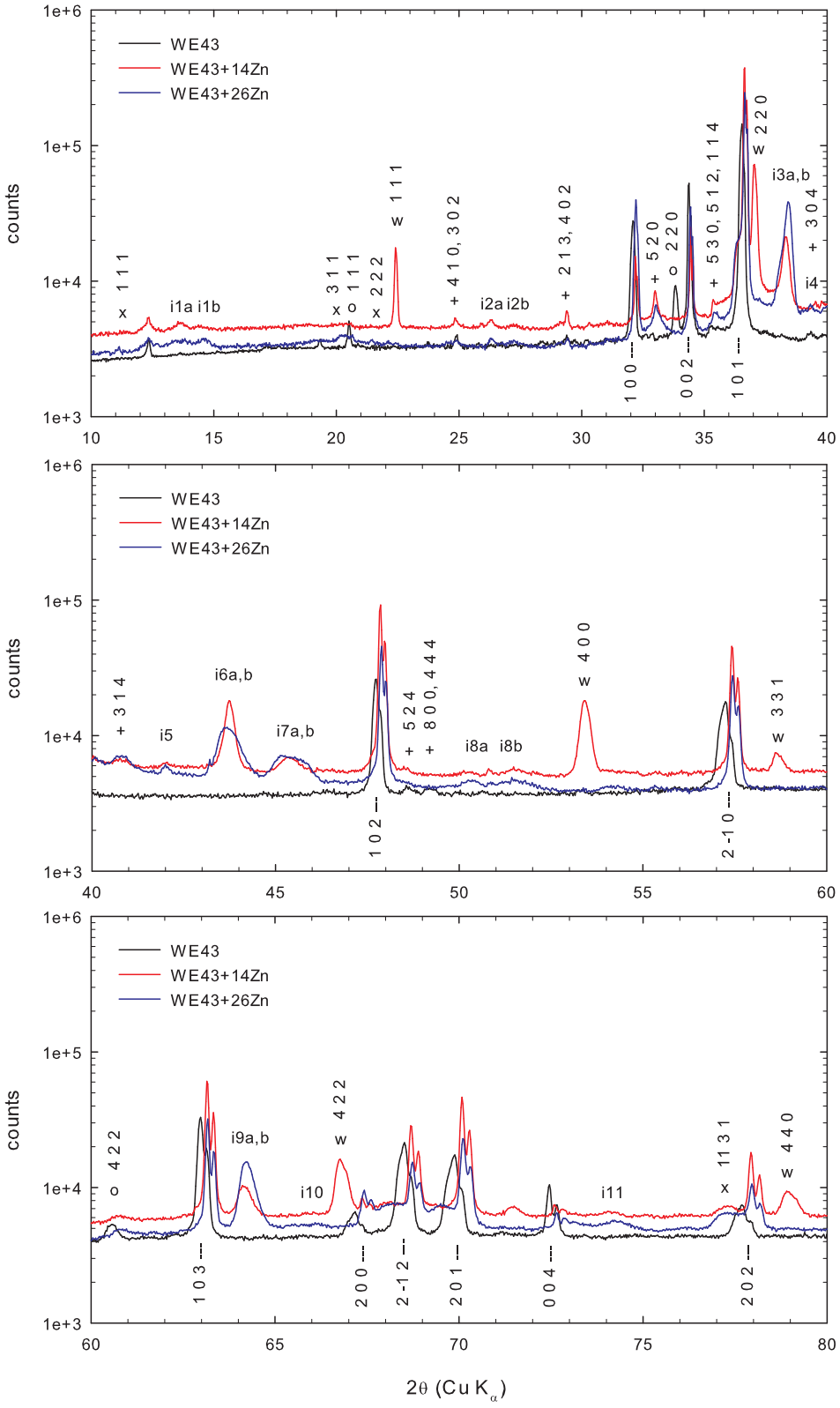

Figure 4.16: X-ray diffractograms of WE43-based alloys, 2θ = 10 - 80°. | - Mg matrix; + - $Mg_{41}Nd_5$ tetragonal phase; o - $Mg_5Nd_{0.4}Y_{0.6}$ fcc phase; x - Mg_7Zn_3 fcc phase; w - $Mg_3Zn_3Y_2$ fcc phase; i - $Mg_3Zn_6Y_1$ icosahedral phase.

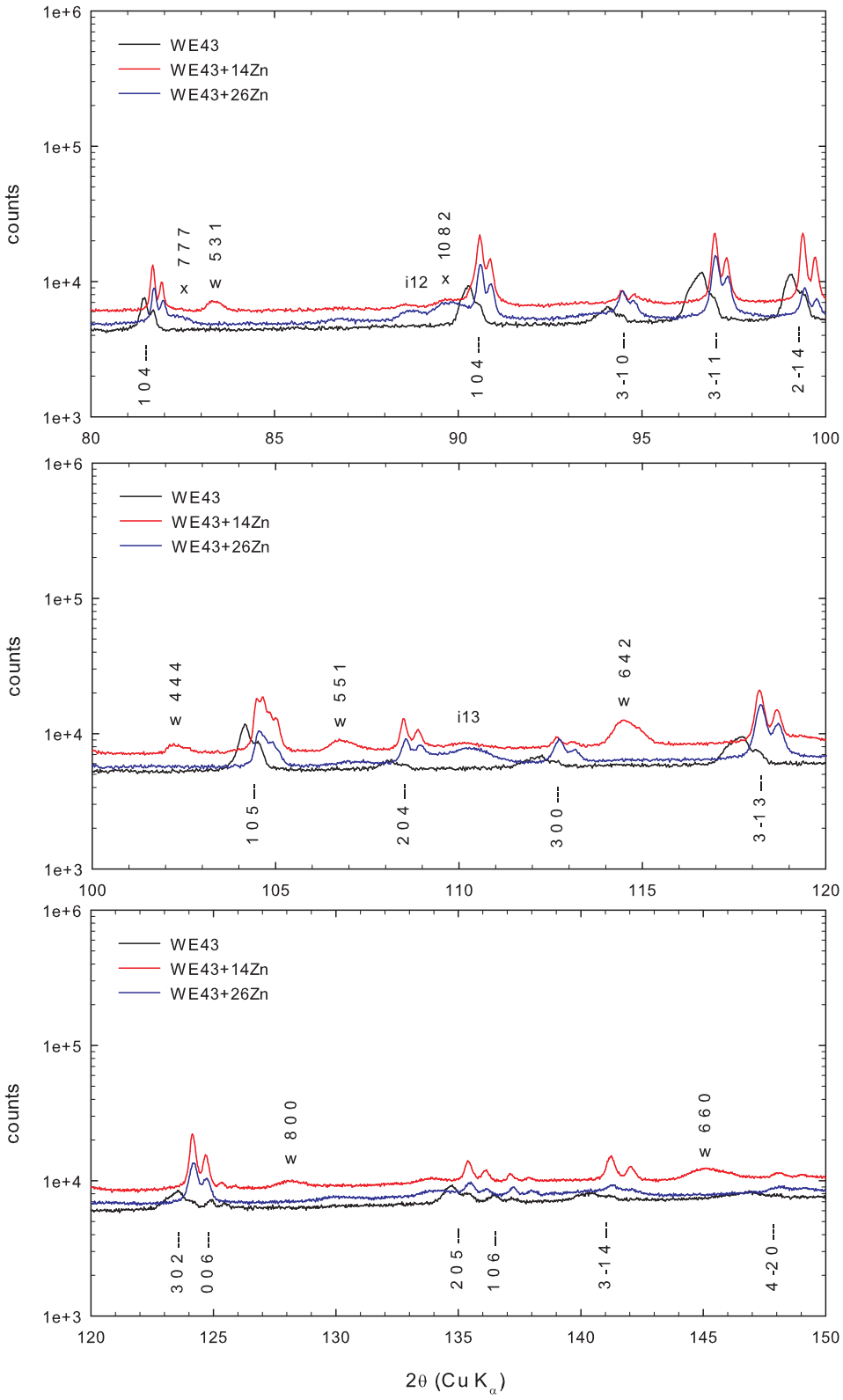

Figure 4.17: X-ray diffractograms of WE43-based alloys, 2θ = 80 - 150°. | - Mg matrix; + - $Mg_{41}Nd_5$ tetragonal phase; o - $Mg_5Nd_{0.4}Y_{0.6}$ fcc phase; x - Mg_7Zn_3 fcc phase; w - $Mg_3Zn_3Y_2$ fcc phase; i - $Mg_3Zn_6Y_1$ icosahedral phase.

4.2.3 Defect studies

LT measurements were performed on as-cast samples of WE43-based alloys. Results of LT measurements are shown in table 4.8. LT spectrum of WE43 alloy exhibit single component with lifetime τ_1 which agrees well with the magnesium bulk positron lifetime of $\sim$ 225 ps [23]. Therefore, we can conclude that concentration of trapping sites in WE43 alloy is lower than detection threshold of positron lifetime spectroscopy.

LT spectra of WE43+14Zn and WE43+26Zn alloys consist of two components. The lifetime of the first component τ_1 is shortened due to positron trapping in defects. The second component with lifetime $\tau_2 \sim 302$ ps represents a contribution of positrons trapped at vacancy-like defects.

Results of LT investigations were analyzed by application of STM. The lifetime τ_B was determined using equation (2.23) to check applicability of STM in this case. Calculated values of τ_B are in good agreement with the bulk positron lifetime of well-annealed magnesium $\sim$ 225 ps. This testifies that assumptions of STM are fulfilled and therefore concentration of defects in WE43+14Zn and WE43+26Zn alloys can be determined by STM.

Positron trapping rate K_D was calculated from equation (2.21). Concentration of defects c_D was determined from the positron trapping rate K_D using equation (2.22). Calculated positron trapping rate and concentration of defects are shown in table 4.8. The positron specific trapping rate ν_D to vacancies in metals usually falls into the range $10^{14} - 10^{15}$ s^{-1} [24]. The value $\nu_D = 10^{14}$ s^{-1} was used to estimate the concentration of vacancy-like defects in WE43-based alloys. The choice of this value is explained in section 4.1.3.

	τ_1 (ps)	I_1 (%)	τ_2 (ps)	I_2 (%)	τ_B (ps)	K_D (10^8s^{-1})	c_D
WE43	223.9(3)	100	-	-	-	-	-
WE43+14Zn	187(2)	55(2)	302(3)	45(2)	226(4)	9.1(1)	9.1(1)$\times 10^{-6}$
WE43+26Zn	192(4)	56(3)	302(4)	44(3)	228(5)	8.3(2)	8.3(2)$\times 10^{-6}$

Table 4.8: Results of LT measurements of WE43-based alloys.

CDB investigations were performed on as-cast samples of WE43-based alloys. Measured CDB ratio curves are shown in figure 4.18. In the high momentum region where the contribution of positrons annihilated by core electron dominates the ratio curve ρ related to well-annealed Mg measured on WE43-based alloys can be expressed as linear combination

$$\begin{aligned}\rho = (1 - F_D)(\xi_{Mg,B} + \xi_{Zn,B}\rho_{Zn,B} + \xi_{Y,B}\rho_{Y,B} + \xi_{Nd,B}\rho_{Nd,B}) + \\ + F_D\ (\xi_{Mg,D}\rho_{Mg,D} + \xi_{Zn,D}\rho_{Zn,D} + \xi_{Y,D}\rho_{Y,D} + \xi_{Nd,D}\rho_{Nd,D}),\end{aligned} \tag{4.4}$$

where F_D is the fraction of positrons trapped at the defects. $\rho_{Zn,B}$, $\rho_{Y,B}$ and $\rho_{Nd,B}$ are the ratio curves of free positrons annihilated by Zn, Y and Nd electrons, respectively. The symbols $\rho_{Mg,D}$, $\rho_{Zn,D}$, $\rho_{Y,D}$ and $\rho_{Nd,D}$ denote the ratio curves for positrons trapped at defects and annihilated by Mg, Zn, Y and Nd electrons, respectively. The coefficients $\xi_{Mg,B}$, $\xi_{Zn,B}$, $\xi_{Y,B}$ and $\xi_{Nd,B}$ represent the fraction of free positrons annihilated by Mg, Zn, Y and Nd electrons, respectively. These coefficients fulfill the normalization condition $\xi_{Mg,B}+\xi_{Zn,B}+\xi_{Y,B}+\xi_{Nd,B} = 1$. The

coefficients $\xi_{Mg,D}$, $\xi_{Zn,D}$, $\xi_{Y,D}$ and $\xi_{Nd,D}$ denote the fraction of positrons trapped at defects and annihilated by Mg, Zn, Y and Nd electrons, respectively. These coefficients again fulfill the normalization condition $\xi_{Mg,D}+\xi_{Zn,D}+\xi_{Y,D}+\xi_{Nd,D} = 1$.

All ratio curves are related to the reference spectrum of well-annealed magnesium. The reference ratio curve $\rho_{Mg,D}$ is shown in figure 4.9 and the ratio curves $\rho_{Zn,B}$ and $\rho_{Zn,D}$ are plotted in figure 4.10. The ratio curves $\xi_{Y,B}$, $\xi_{Y,D}$, $\xi_{Nd,B}$ and $\xi_{Nd,D}$ were determined by measuring reference samples of well-annealed and cold rolled Y and Nd samples.

In the well-annealed samples annihilation of all positron occur from the free state. The CDB ratio curve of cold rolled Y can be expressed as (see section 4.1.3 for detailed explanation)

$$\rho = (1 - F_D)\rho_{Y,B} + F_D\rho_{Y,D}. \tag{4.5}$$

The ratio curve $\rho_{Y,D}$ was detemined from equation 4.5 using the fraction F_D obtained from LT measurement of the cold rolled Y sample. The CDB ratio curve of cold rolled Nd can be expressed analogically as

$$\rho = (1 - F_D)\rho_{Nd,B} + F_D\rho_{Nd,D}, \tag{4.6}$$

where F_D was obtained by LT measurement of the cold rolled Nd sample. Reference CDB ratio curves of Y and Nd are plotted in figures 4.19 and 4.20, respectively.

Fractions ξ for each reference ratio curve and the fraction of positrons trapped at the defects F_D were obtained by fitting of measured CDB ratio curves of WE43-based alloys using equation (4.4). Results of fitting are shown in table 4.9. Example of fitted CDB ratio curve is shown in figure 4.21.

In the case of WE43 alloy the fractions $\xi_{Zn,B}$ and $\xi_{Zn,D}$ were fixed at zero value, because WE43 alloy does not contain zinc. It is reasonable to assume that certain amount of zinc was disolved in Mg matrix during casting of WE43 alloys modified by addition of Zn. Presence of Zn dissolved in Mg matrix is testified by a shift of Mg reflections in X-ray diffractograms with respect to their original positions in WE43 alloy, see figure 4.16.

This shift is practically the same in both WE43+14Zn and WE43+26Zn alloys despite various Zn content. This suggest that saturated solid solution of Zn in Mg was formed in both alloys. To reduce the number of free parameters in fitting the fraction $\xi_{Zn,B}$ was fixed at the limit of solubility of zinc in magnesium 2.3 at.% in the case of WE43+14Zn and WE43+26Zn alloys.

All samples of WE43-based alloys exhibit a peak in the ratio curves at 8×10^{-3} m_0c. This represents contribution of 4f electrons present in rare-earth (RE) elements, i.e., Y and Nd. In addition the WE43 alloys modified by Zn addition exhibit also a broad peak centered at 18×10^{-3} m_0c which comes from positrons annihilated by 3d Zn electrons, see figure 4.10. Since fitted fraction of positrons annihilated by electrons of RE elements is substantially higher than average content of Y and Nd in the samples obtained from chemical analysis, positrons must annihilate in the RE-rich phases.

The CDB ratio curve (related to well-annealed by Mg) measured on WE43

alloy can be described as

$$\rho = (1 - F_D)(\xi_{Mg,B} + \xi_{Y,B}\rho_{Y,B} + \xi_{Nd,B}\rho_{Nd,B}) + \\ + F_D\ (\xi_{Mg,D}\rho_{Mg,D} + \xi_{Y,D}\rho_{Y,D} + \xi_{Nd,D}\rho_{Nd,D}). \tag{4.7}$$

The best fit using equation (4.7) is plotted in figure 4.18 by solid line and the fractions $\xi_{Mg,B}$, $\xi_{Y,B}$, $\xi_{Nd,B}$, $\xi_{Mg,D}$, $\xi_{Y,D}$, $\xi_{Nd,D}$, and F_D are listed in table 4.9.

Positrons in WE43 alloy annihilate predominantly in Mg matrix but certain fraction of positrons annihilate from localized state at Nd-rich precipitates. These Nd-rich particles are apparently finely dispersed precipitates of $Mg_{41}Nd_5$ phase identified in WE43 sample by XRD, see table 4.6. Since only a single component with lifetime of $\sim$ 225 ps was found in LT spectra of WE43 sample, there are probably no open-volume defects associated with $Mg_{41}Nd_5$ phase but positrons are localized directly inside $Mg_{41}Nd_5$ particles due to higher absolute value of positron affinity compared to Mg matrix.

Hence, lifetime of positrons localized in $Mg_{41}Nd_5$ phase is comparable to that of free positrons in Mg matrix and contribution of positrons localized in $Mg_{41}Nd_5$ precipitates can be distinguished from those annihilated in Mg matrix only by CDB measurement through enhanced contribution of annihilations with Nd electrons. One can see in figure 4.18 that agreement of the best fit by equation (4.7) with experimental CDB ratio curve for WE43 alloy is not perfect. This discrepancy is probably caused by some impurities unaccounted for in equation (4.4).

The CDB ratio curves of WE43 alloys modified by addition of Zn can be described as superposition of the following contributions

$$\rho = (1 - F_D)(\xi_{Mg,B} + \xi_{Zn,B}\rho_{Zn,B} + \xi_{Y,B}\rho_{Y,B} + \xi_{Nd,B}\rho_{Nd,B}) + \\ + F_D\ (\xi_{Mg,D}\rho_{Mg,D} + \xi_{Zn,D}\rho_{Zn,D} + \xi_{Y,D}\rho_{Y,D} + \xi_{Nd,D}\rho_{Nd,D}). \tag{4.8}$$

One can see that model curves calculated by equation (4.8) and plotted figure 4.18 by solid lines are in very reasonable agreement with experiment. The fractions of positrons annihilated by various kinds of electrons obtained from the best fit are listed in table 4.9.

It is clear that environment of vacancy like defects characterized by lifetime of $\sim$ 300 ps contains substantially enhanced concentration of Zn and Y. This is most pronounced in the case of WE43+26Zn where virtually all positrons trapped at vacancy-like defects are annihiled by Zn or Y electrons. This results supports the picture that vacancy-like defects are associated with icosahedral phase $Mg_3Zn_6Y_1$ characterized by high Zn and Y content.

	$\xi_{Mg,B}$	$\xi_{Zn,B}$	$\xi_{Y,B}$	$\xi_{Nd,B}$	$\xi_{Mg,D}$	$\xi_{Zn,D}$	$\xi_{Y,D}$	$\xi_{Nd,D}$	F_D
WE43	98.8(5)	-	0.8(5)	0.4(1)	20(2)	-	0(2)	80(2)	25(2)
WE43+14Zn	96.5(5)	2.3 Fix	1.0(5)	0.2(1)	51(3)	19(3)	30(3)	0(3)	16(1)
WE43+26Zn	96.5(5)	2.3 Fix	1.0(5)	0.2(1)	0(4)	54(4)	46(4)	0(4)	16(1)

Table 4.9: Results of CDB measurements of WE43-based alloys.

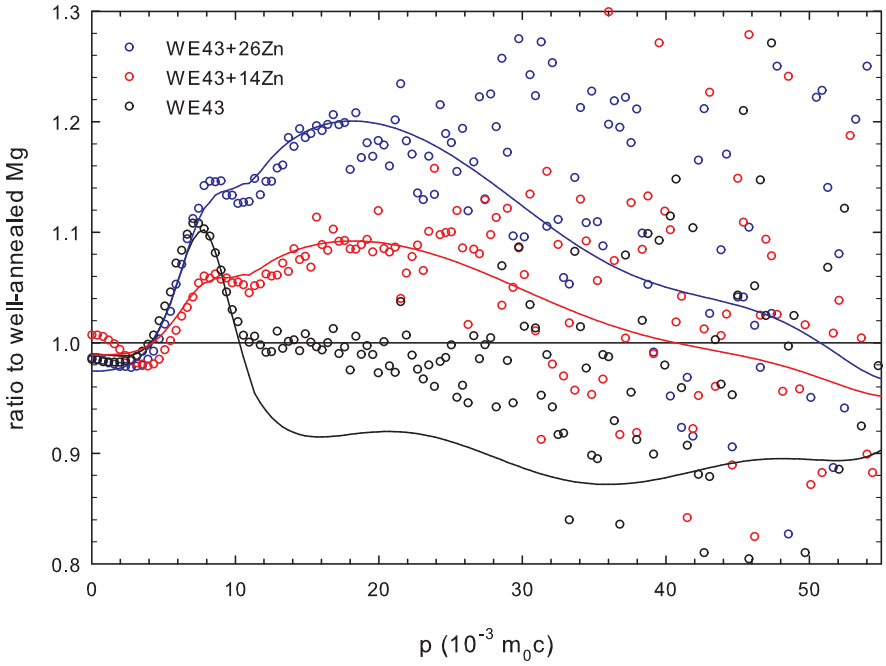

Figure 4.18: CDB ratio curves (related to well-annealed Mg) of WE43-based alloys. Open circles - measured data; lines - fit.

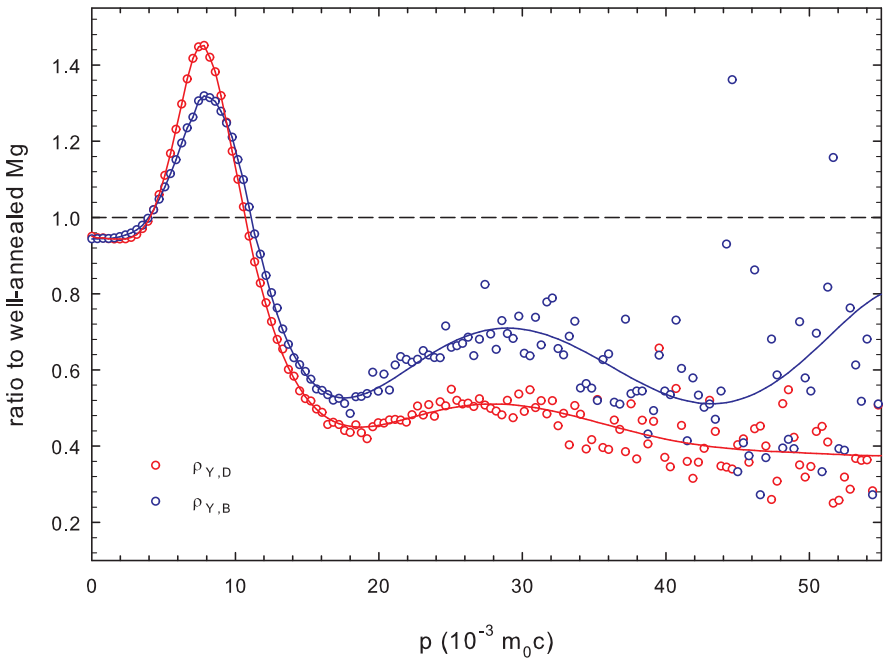

Figure 4.19: Reference ratio curves (related to well-annealed Mg) for ratio curves of free positrons annihilated by Y electrons $\rho_{Y,B}$ and positrons trapped at defects and annihilated by Y electrons $\rho_{Y,D}$.

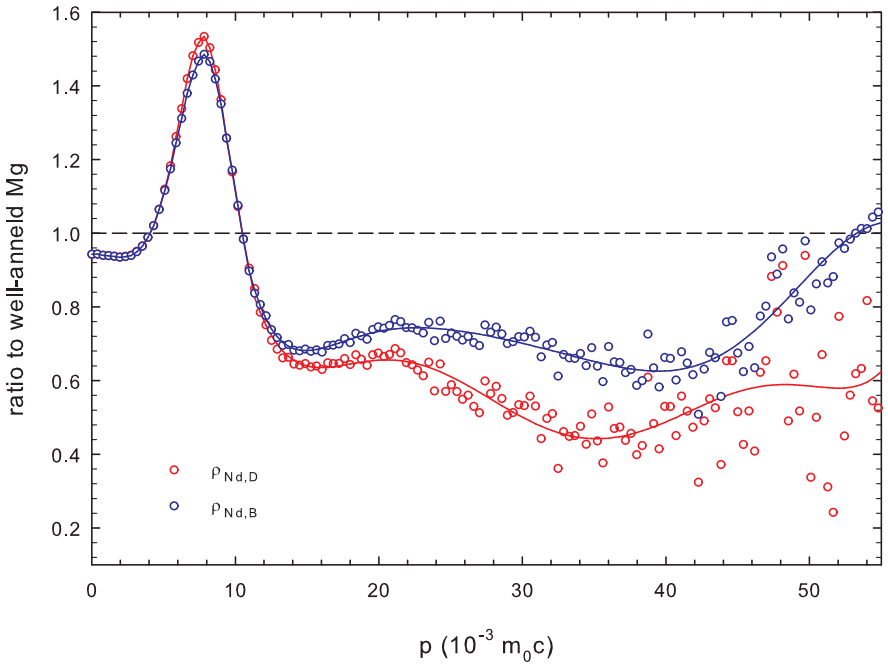

Figure 4.20: Reference ratio curves (related to well-annealed Mg) for ratio curves of free positrons annihilated by Nd electrons $\rho_{Nd,B}$ and positrons trapped at defects and annihilated by Nd electrons $\rho_{Nd,D}$.

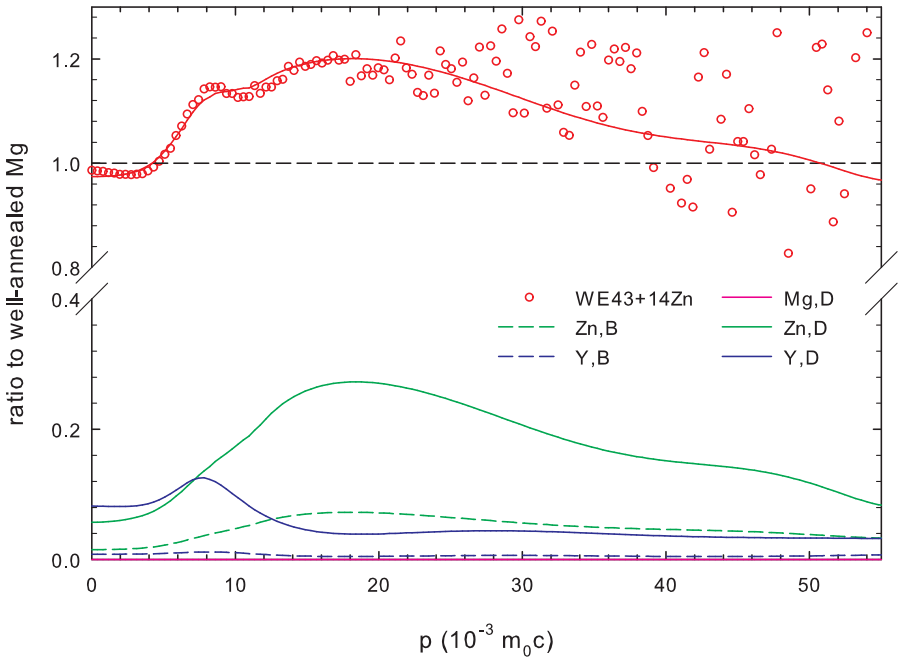

Figure 4.21: Fitted CDB ratio curve (related to well-annealed Mg) of WE43+14Zn alloy. Open circles - measured data; lines - components of the fit.

4.3 MgZnAl-based alloys

4.3.1 Samples

Samples of MgZnAl and MgZnAlCa alloys were prepared by squeeze casting. Their compositions were determined by chemical analysis and are shown in tables 4.10 and 4.11.

	Zn	Al	Ca	Mg
MgZnAl	11.52	3.04	0.008	balance
MgZnAlCa	5.07	3.29	0.12	balance

Table 4.10: Chemical composition in wt.% of the MgZnAl-based alloys.

	Zn	Al	Ca	Mg
MgZnAl	4.63	2.96	0.005	balance
MgZnAlCa	1.95	3.07	0.08	balance

Table 4.11: Chemical composition in at.% of the MgZnAl-based alloys.

4.3.2 Mechanical properties and phase composition

Vickers hardness tests were done for both samples and measured values are shown in table 4.12. MgZnAl sample is significantly harder than MgZnAlCa alloy. SEM images of the samples are shown in figures 4.22 to 4.24. Eutectic is formed around grain boundaries and contrary to WE43-based alloys it does not exhibit lamellar structure. Detail of the eutectic is shown in figure 4.23.

Results of volume fraction analysis of SEM images are shown in table 4.13. MgZnAl alloy exhibits higher volume fraction fraction of eutectic compared to MgZnAlCa sample. Except of the eutectic phase one can observe bands with enhanced Zn content along grain boudaries. These bands are more pronounced in MgZnAlCa alloy which exhibits lower volume fraction of the eutectic. Separate hardness measurements in matrix and in eutectic were not possible in MgZnAl-based alloys due to low volume fraction of the eutectic.

	MgZnAl	MgZnAlCa
HV0.1	100 ± 2	83 ± 2

Table 4.12: Hardness of MgZnAl-based alloys.

	MgZnAl	MgZnAlCa
vol. frac. of eutectic (%)	6.2 ± 0.3	3.4 ± 0.2

Table 4.13: Volume fraction of the eutectic in MgZnAl-based alloys.

Phase composition of the samples was determined by XRD measurements. Diffractograms of the studied samples are shown in figures 4.25 and 4.26. Following phases except of the magnesium matrix were identified: body-centered cubic (BCC) $Mg_{17}Al_{12}$ phase and the icosahedral $Mg_{44}Zn_{41}Al_{15}$ phase. Peaks corresponding to each identified phase were fitted by pseudo-Voigt function. Calculated lattice parameters of $Mg_{17}Al_{12}$ phase are shown in table 4.14.

	MgZnAl	MgZnAlCa
$Mg_{17}Al_{12}$ - bcc	a = 10.65(2) Å	a = 10.75(5) Å

Table 4.14: Lattice parameters of $Mg_{17}Al_{12}$ phase present in MgZnAl-based alloys.

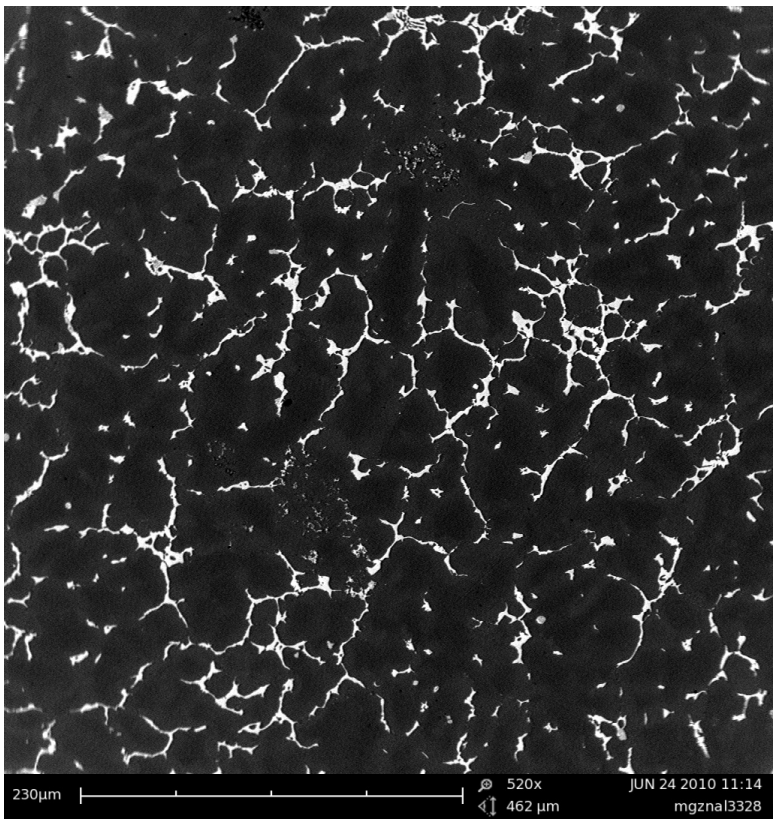

Figure 4.22: SEM image of as-cast MgZnAl alloy.

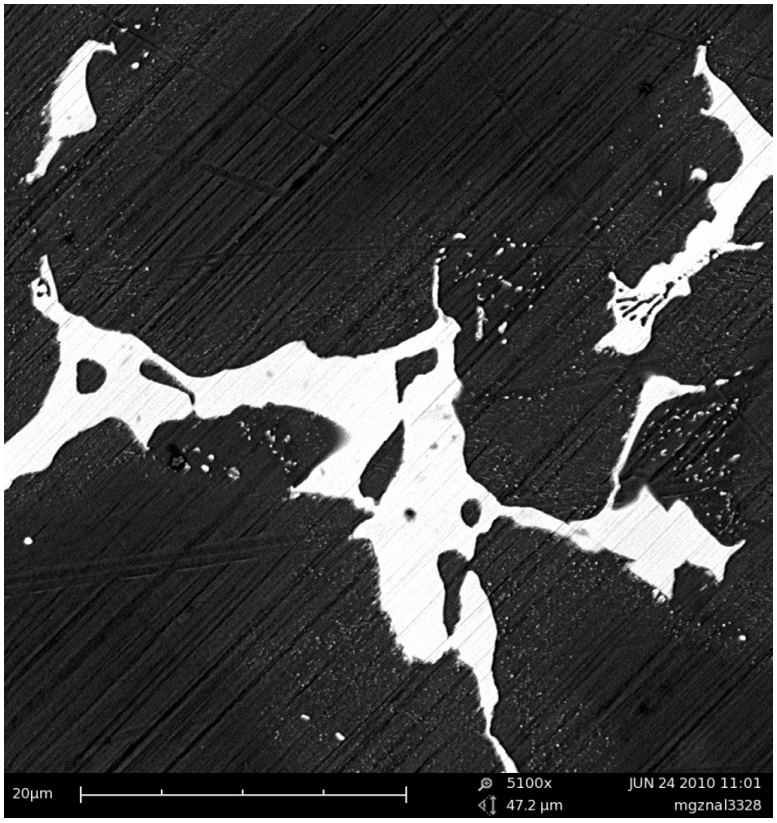

Figure 4.23: SEM image of as-cast MgZnAl, detail of the eutectic phase.

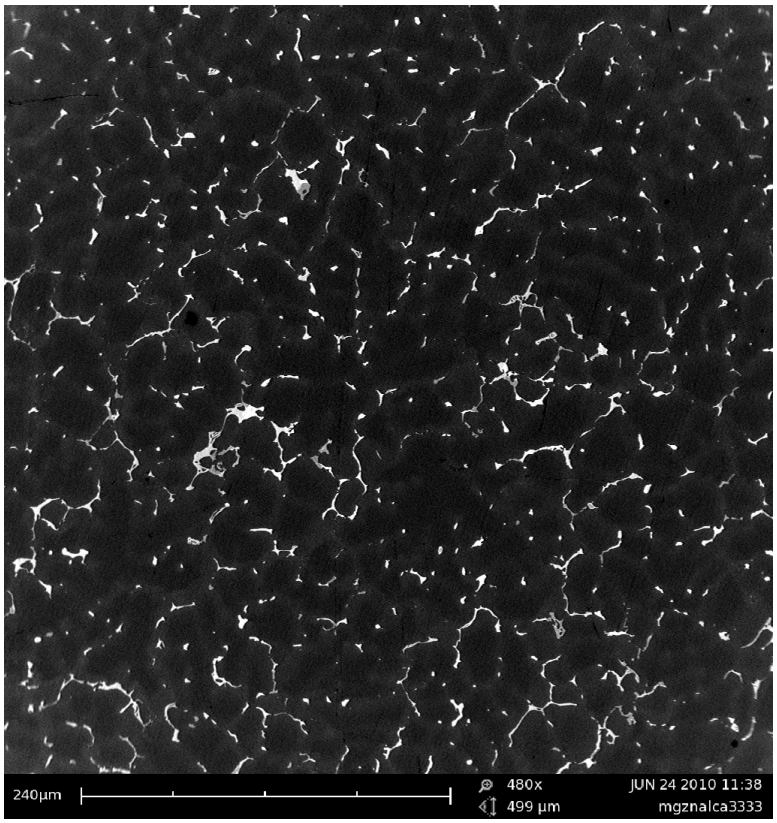

Figure 4.24: SEM image of as-cast MgZnAlCa alloy.

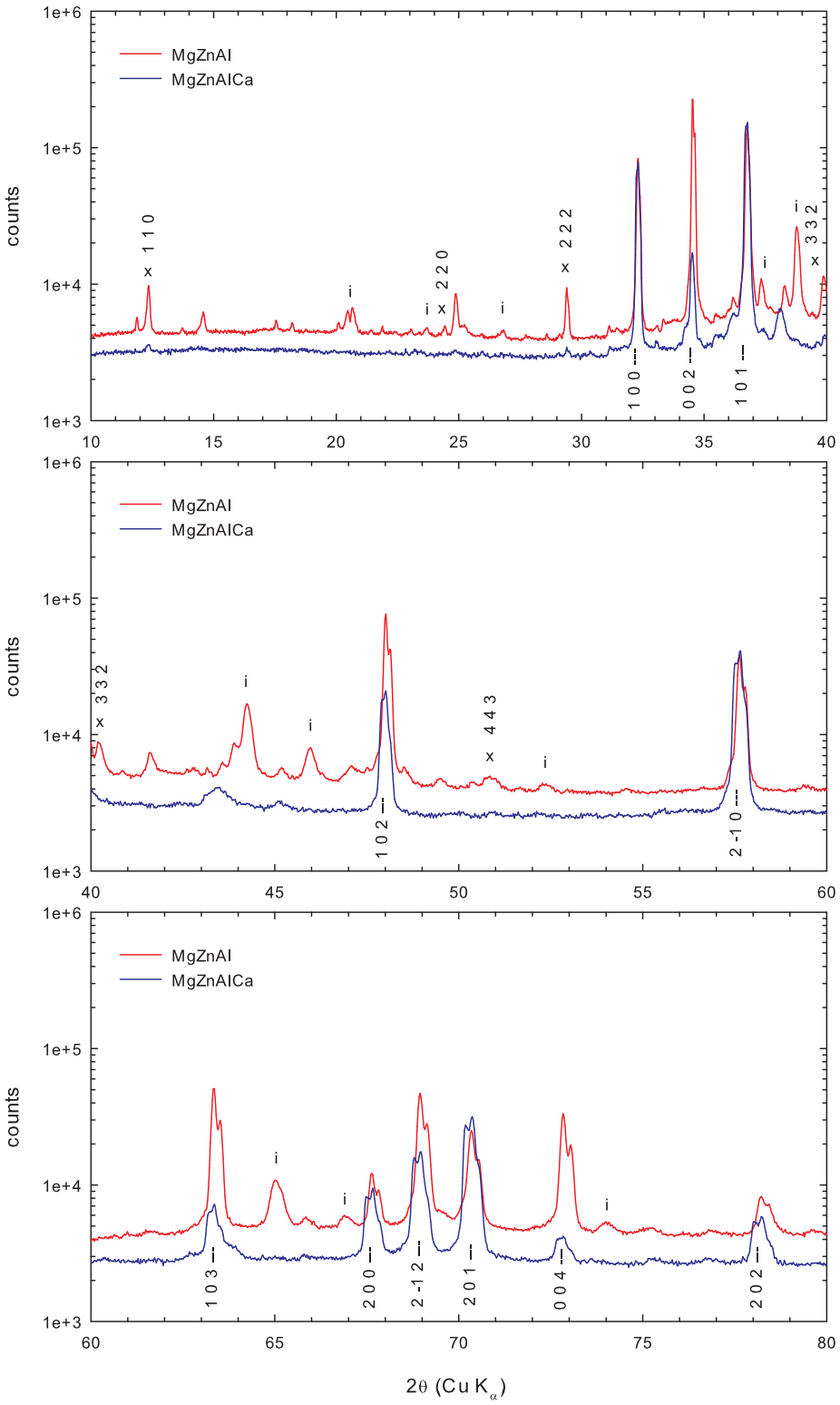

Figure 4.25: X-ray diffractograms of MgZnAl-based alloys, 2θ = 10 - 80°. | - Mg matrix; x - $Mg_{17}Al_{12}$ bcc phase; i - $Mg_{44}Zn_{41}Al_{15}$ icosahedral phase.

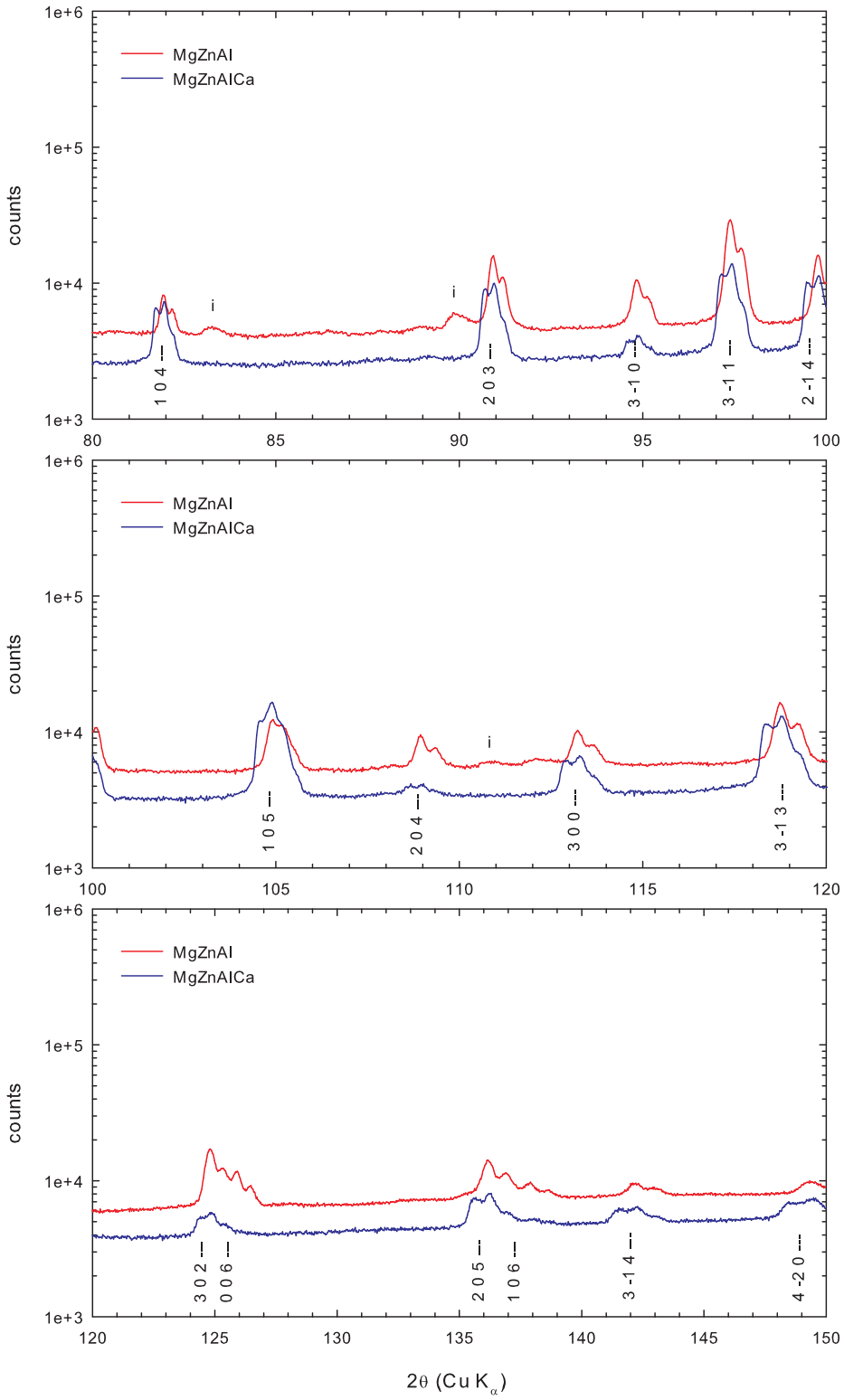

Figure 4.26: X-ray diffractograms of MgZnAl-based alloys, 2θ = 80 - 150°. | - Mg matrix; x - $Mg_{17}Al_{12}$ bcc phase; i - $Mg_{44}Zn_{41}Al_{15}$ icosahedral phase.

4.3.3 Defect studies

LT measurements were performed on the samples of MgZnAl-based alloys. Results of LT measurements are shown in table 4.15. Both samples exhibit single component LT spectra with positron lifetime $\tau_1 \sim 220$ ps. This value of lifetime τ_1 is slightly lower than bulk positron lifetime τ_B of well-annealed magnesium of ~ 225 ps [23].

Many quasicrystals exhibit single component spectra with positron lifetime of ~ 210 ps [28]. However, due to limited resolution of LT spectrometer, it is not possible to distinguish components with such similar lifetimes. Therefore, the component with average lifetime τ_1 between 210 and 225 ps is observed in measured LT spectra. Since all LT spectra exhibit single component, STM cannot be used to estimate concentration of eventual defects.

	τ_1 (ps)	I_1 (%)	K_D (ps^{-1})	c_D
MgZnAl	219.5(3)	100	-	-
MgZnAlCa	220.8(5)	100	-	-

Table 4.15: Results of LT measurements of MgZnAl-based alloys.

CDB investigations were performed on the samples of MgZnAl-based alloys. Measured ratio curves are shown in figure 4.27. In the high momentum region where the contribution of positrons annihilated by core electron dominates the ratio curve ρ (related to well-annealed Mg) measured on MgZnAl-based alloys can be expressed as linear combination

$$\begin{aligned}\rho = (1 - F_D)(\xi_{Mg,B} + \xi_{Zn,B}\rho_{Zn,B} + \xi_{Al,B}\rho_{Al,B}) + \\ + F_D\ (\xi_{Mg,D}\rho_{Mg,D} + \xi_{Zn,D}\rho_{Zn,D} + \xi_{Al,D}\rho_{Al,D}),\end{aligned} \tag{4.9}$$

where F_D is the fraction of trapped positrons. $\rho_{Zn,B}$ and $\rho_{Al,B}$ are the ratio curves of free positrons annihilated by Zn and Al electrons, respectively. $\rho_{Mg,D}$, $\rho_{Zn,D}$ and $\rho_{Al,D}$ are the ratio curves for trapped positrons annihilated by Mg, Zn and Al electrons, respectively. The coefficients $\xi_{Mg,B}$, $\xi_{Zn,B}$ and $\xi_{Al,B}$ represent the fraction of free positrons annihilated by Mg, Zn and Al electrons, respectively. These coefficients fulfill the normalization condition $\xi_{Mg,B} + \xi_{Zn,B} + \xi_{Al,B} = 1$. The coefficients $\xi_{Mg,D}$, $\xi_{Zn,D}$ and $\xi_{Al,D}$ denote the fraction of trapped positrons annihilated by Mg, Zn and Al electrons, respectively. These coefficients again fulfill the normalization condition $\xi_{Mg,D} + \xi_{Zn,D} + \xi_{Al,D} = 1$.

The ratio curves $\rho_{Al,B}$ and $\rho_{Al,D}$ were determined by measuring reference samples of well-annealed and cold rolled aluminium. In the well-annealed samples annihilations of all positrons occur from the free state, i.e. the corresponding ratio curve equals $\rho_{Al,B}$.

The CDB ratio curve of cold rolled Al can be expressed as (see section 4.1.3 for detailed explanation)

$$\rho = (1 - F_D)\rho_{Al,B} + F_D\rho_{Al,D}, \tag{4.10}$$

where fraction of positrons trapped at defects F_D was obtained by LT measurement of the cold rolled Al sample.

Reference CDB ratio curves of Mg, Zn and Al related to the reference spectrum of well-annealed magnesium are plotted in figures 4.9, 4.10 and 4.28 respectively.

Both samples of MgZnAl and MgZnAlCa alloys exhibit a peak in the ratio curves at $8{\times}10^{-3}$ m_0c, see figure 4.27. This peak represents a contribution of positrons annihilated by core electrons of aluminium, cf. figure 4.28. In the low momentum range ($p < 12 \times 10^{-3}$ m_0c) the shape of the reference Al ratio curves agrees well with that of measured CDB ratio curves for MgZnAl-based alloys.

However, in the high momentum region shape of measured ratio curves significantly differs from that of aluminium. This can be again resolved by combining ratio curves of aluminium and zinc. The ratio curves of well-annealed and deformed zinc exhibit a broad peak in the high momentum region that compensates low values of the ratio curves of aluminium.

While it was not possible to detect eventual positron trapping using LT investigations, the fraction of trapped positrons F_D obtained from fit of measured CDB ratio curves shows that positron trapping occurs in MgZnAl-based alloys. Furthermore, the coefficients $\xi_{Zn,D}$ and $\xi_{Al,D}$ listed in table 4.16 obtained from fitting of experimental ration curves by equation (4.9) show that environment of positron trapping sites is rich in zinc and aluminium. This strongly suggests that certain fraction of positrons is annihilated in $Mg_{44}Zn_{41}Y_{15}$ quasicrystalline phase. Example of fitted CDB ratio curve is shown in figure 4.29.

	$\xi_{Mg,B}$	$\xi_{Zn,B}$	$\xi_{Al,B}$	$\xi_{Mg,D}$	$\xi_{Zn,D}$	$\xi_{Al,D}$	F_D
MgZnAl	94.8(5)	2.3 Fix	2.9(3)	5(2)	20(2)	75(2)	10(1)
MgZnAlCa	95.5(5)	1.5(2)	3.0(5)	7(2)	18(2)	75(2)	11(1)

Table 4.16: Results of CDB measurements of MgZnAl-based alloys.

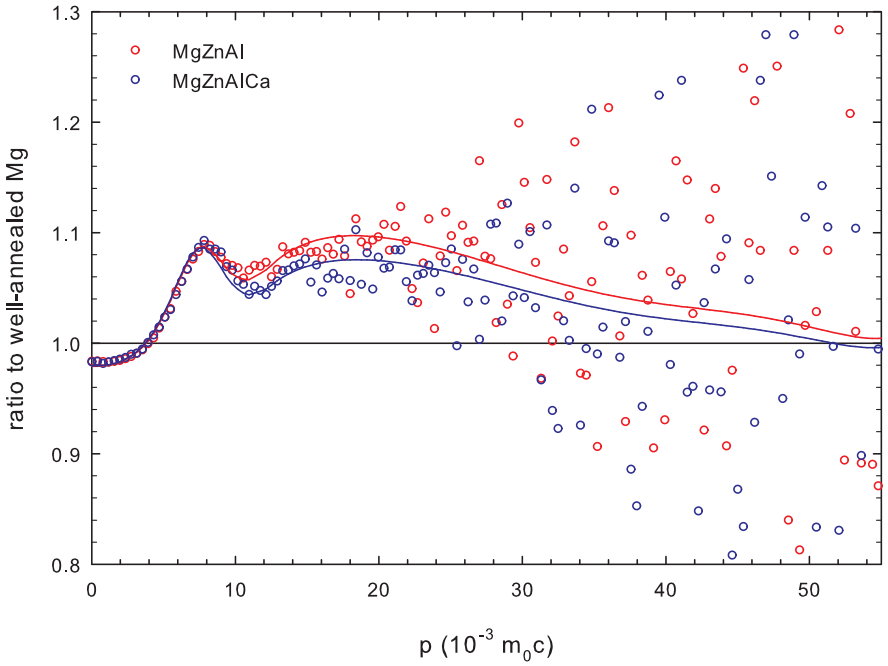

Figure 4.27: CDB ratio curves (related to well-annealed Mg) of MgZnAl-based alloys. Fit of the CDB ratio curves by equation (4.9) is plotted by solid lines.

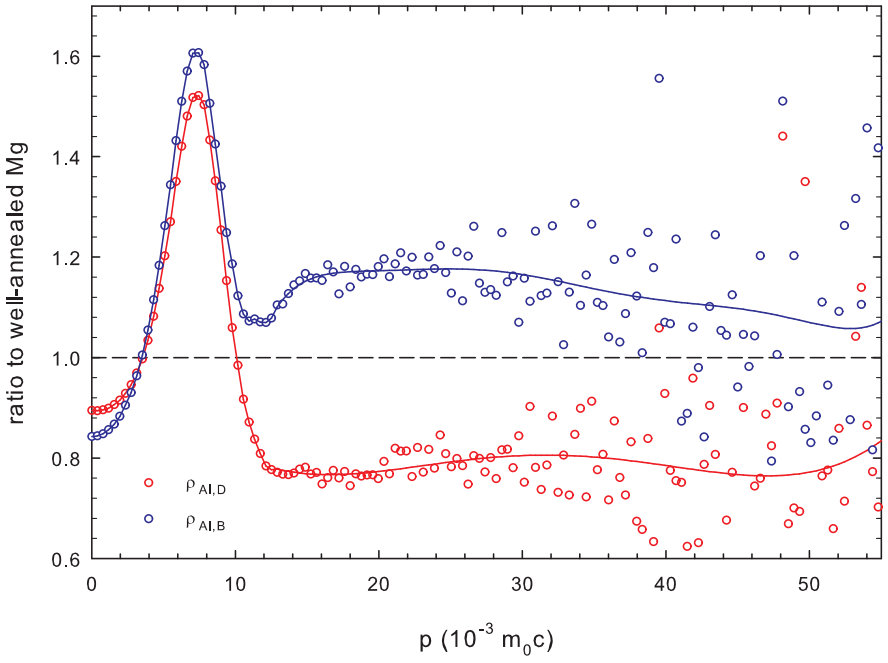

Figure 4.28: CDB ratio curves (related to well-annealed Mg) of well-annealed and deformed aluminium.

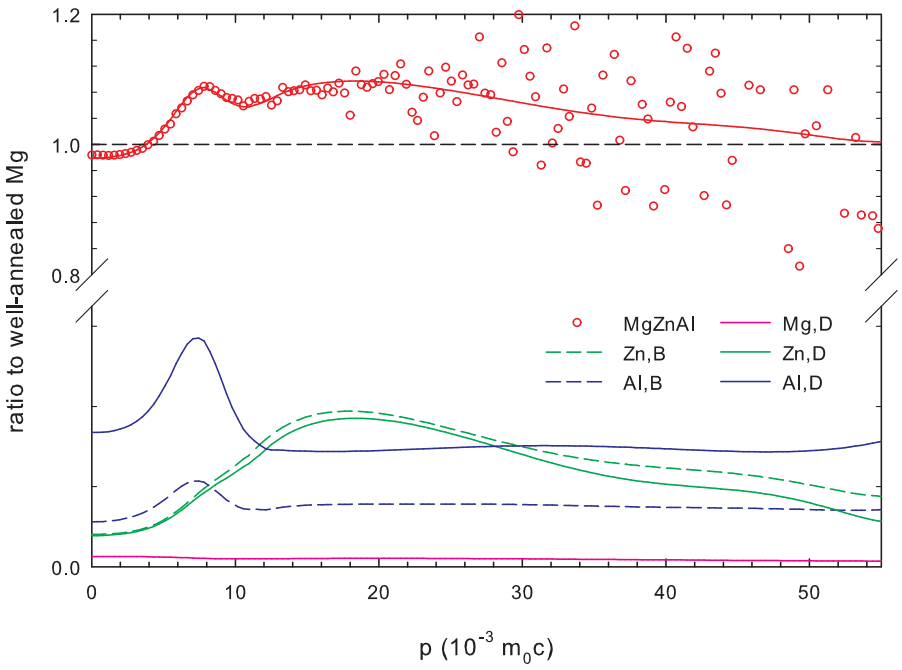

Figure 4.29: Fitted CDB ratio curve (related to well-annealed Mg) of MgZnAl alloy. Open circles - measured data; lines - components of the fit.

5. Discusion

5.1 Model binary alloy Mg6Zn

SEM investigations revealed, that as-cast Mg6Zn alloy is not homogenous and contains diffuse areas with higher zinc content around grain boundaries and also some undissolved zinc-rich particles. At higher anealing temperatures zinc distribution in the sample becomes more homogenous and zinc-rich particles are disolved in the matrix.

This process can be observed on SEM images shown in figures 4.3, 4.4 and 4.5 obtained from the as-cast sample, the sample annealed at 300 °C for 100 min and the sample annealed at 500 °C for 30 min, respectively.

The composition of investigated Mg6Zn alloy approximately corresponds to the maximum solubility of Zn in Mg which is reached at 340 °C. Below this temperature Zn solubility is significantly lower. Formation of Zn-rich precipitates was detected in the temperature range 210–250 °C by LT and CDB and also by microhardness testing. Open volume misfit defects were detected at the precipitate-matrix interfaces by LT spectroscopy.

Moreover, an enhanced contribution of positrons annihilated by Zn electrons was detected by CDB in the similar temperature range where the precipitation takes place. The existence of misfit defects testifies that Zn-rich precipitates are semicoherent or incoherent with Mg matrix. HV investigations testified hardening effect connected with precipitation these Zn-rich particles.

From comparison with the equilibrium phase diagram (see figure 4.1) MgZn phase is the most probable candidate for these precipitates. However due to local excess of Zn concentration in the vicinity of grain boundaries one cannot exclude formation of precipitates of Mg_2Zn_3 phase. Another possibility which should be considered as well is formation of some metastable Zn-rich phase which is not included in the equilibrium phase diagram. Unfortunately the Zn-rich phase could not be detected by XRD due to its low volume fraction.

5.2 Comparison of WE43-based and MgZnAl-based alloys

The microhardness HV0.1 and the volume fractions of the eutectic in WE43-based and MgZnAl-based alloys determined from SEM images are shown in figures 5.1 and 5.2, respectively. The highest hardness and also highest volume fraction of eutectic was found in WE43+26Zn alloy, i.e. the alloy with maximum zinc content.

Dependence of the Vickers microhardness and the volume fraction of eutectic on zinc content is shown in figures 5.3 and 5.4, respectively. Obviously both the Vickers microhardness and the volume fraction of eutectic increases with zinc content. Correlation plot of Vickers hardness and the volume fraction of eutectic is shown in figure 5.5. Clearly there is a positive correlation between

microhardness and volume fraction of eutectic. One can see in figure 5.5 that the Vickers microhardness increases approximately linearly with increasing volume fraction of eutectic. This can be easily understood since the eutectic contains icosahedral phase responsible for hardening of the alloy. Hence, higher volume fraction of the eutectic leads also to higher concentration of the icosahedral phase.

Icosahedral phase was observed in all samples of WE43-based and MgZnAl-based alloys except of the sample of WE43 alloy with zero zinc content. This shows that zinc is principal element responsible for creation of quasicrystalline icosahedral phase in magnesium alloys.

Defect studies performed by means of positron annihilation spectroscopy techniques indicate that positron trapping occurs in alloys containing the icosahedral phase. Measured CDB spectra shows that positrons are trapped in the vincity of icosahedral phase in both types of alloys.

However, the nature of positron trapping is quite different in WE43-based and MgZnAl-based alloys. In WE43-based alloys positrons are trapped in open-volume vacany-like defects. On the other hand vacancy-like defects were not detected in MgZnAl-based alloys by LT spectroscopy. In MgZnAl-based alloys positrons are trapped at small precipitates of icosahedral phase. This difference can by caused by following possibilities:

(i) Positrons are trapped at defects associated with precipitate-matrix interface of icosahedral phase. SEM investigations clearly showed that WE43-based alloys exhibit significantly higher volume fraction of the eutectic than MgZnAl-based alloys. Furthermore, the eutectic in WE43-based alloys exhibits lamellar structure, which substantially increases the surface to volume ratio. Significant difference in morphology of the eutectic is clearly visible when comparing SEM images of WE43-based alloys and MgZnAl-based alloys shown in figures 4.15 and 4.23, respectively. Therefore, surface of the icosahedral precipitates in WE43-based alloys is much larger than that of MgZnAl-based alloys. This can lead to the situation, that although vacancy-like defects are present also in MgZnAl-based alloys, their concentration is lower than detection limit of LT measurements.

(ii) Vacancy-like defects are absent in MgZnAl-based alloys. This can be caused by aluminium atoms which could fill the vacancy-like defects present at the interface between the icosahedral phase and Mg matrix.

(iii) Combination of (i) and (ii), i.e. some of the vacancy-like defects are filled with aluminium atoms and concetration of unfilled defects is lower than detection limit of positron lifetime measurements.

However, results presented in this work are not sufficient for decision which of these possibilities occurs.

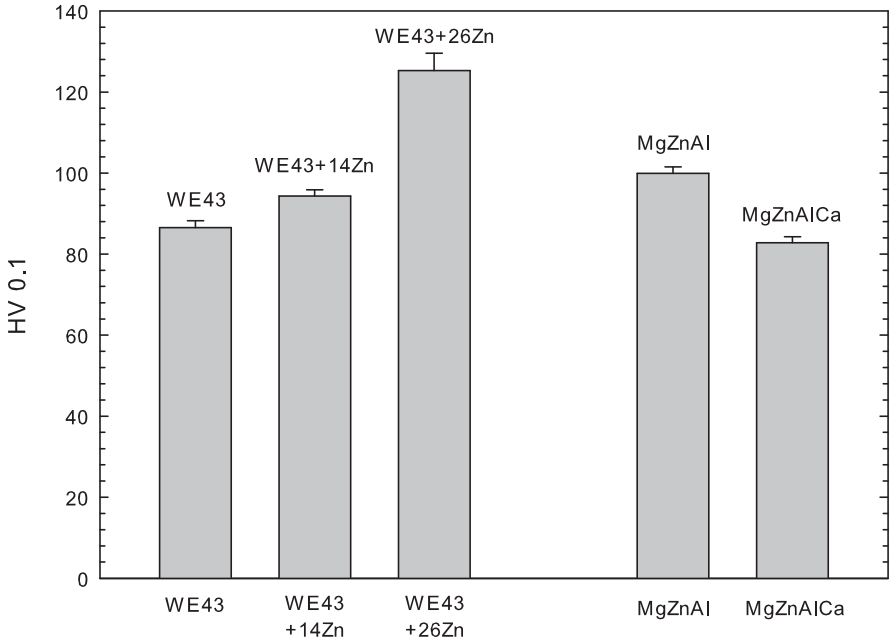

Figure 5.1: Comparison of Vickers hardness of WE43-based and MgZnAl-based alloys.

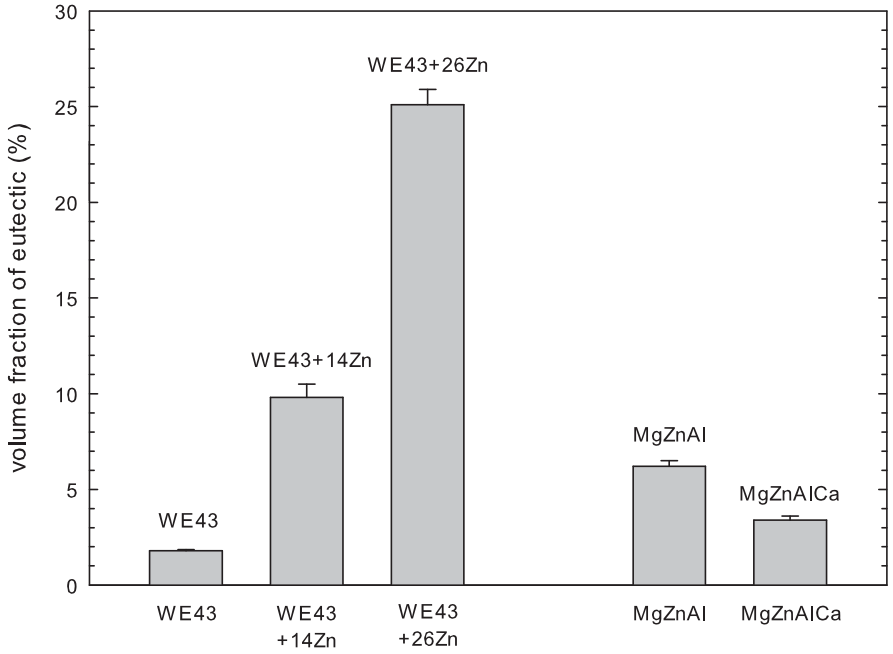

Figure 5.2: Comparison of the volume fraction of eutectic in WE43-based and MgZnAl-based alloys.

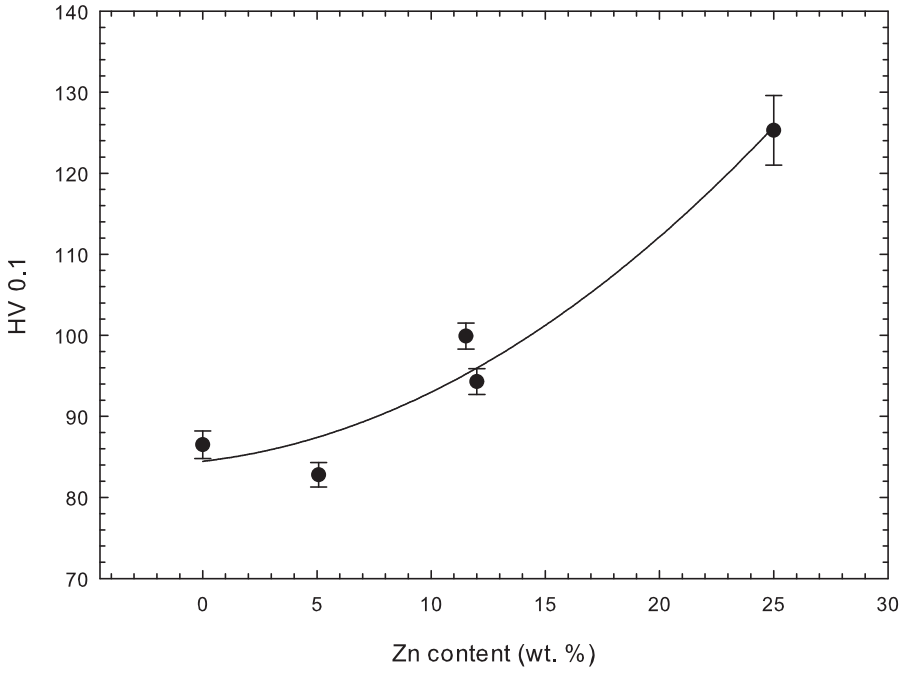

Figure 5.3: Dependence of the Vickers hardness measured on WE43-based and MgZnAl-based alloys on zinc content.

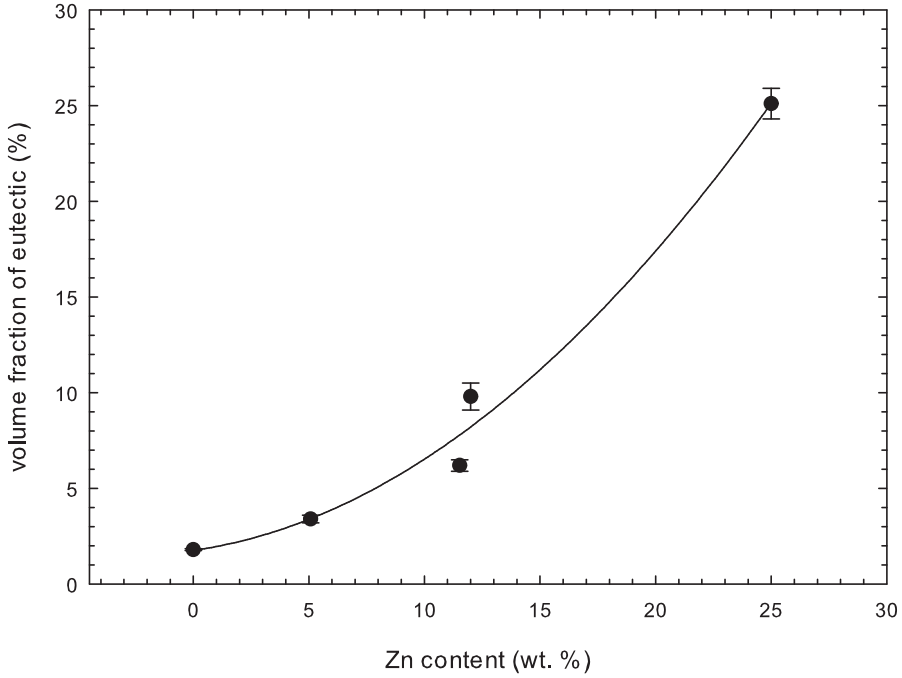

Figure 5.4: Dependence of the volume fraction of eutectic in WE43-based and MgZnAl-based alloys on zinc content.

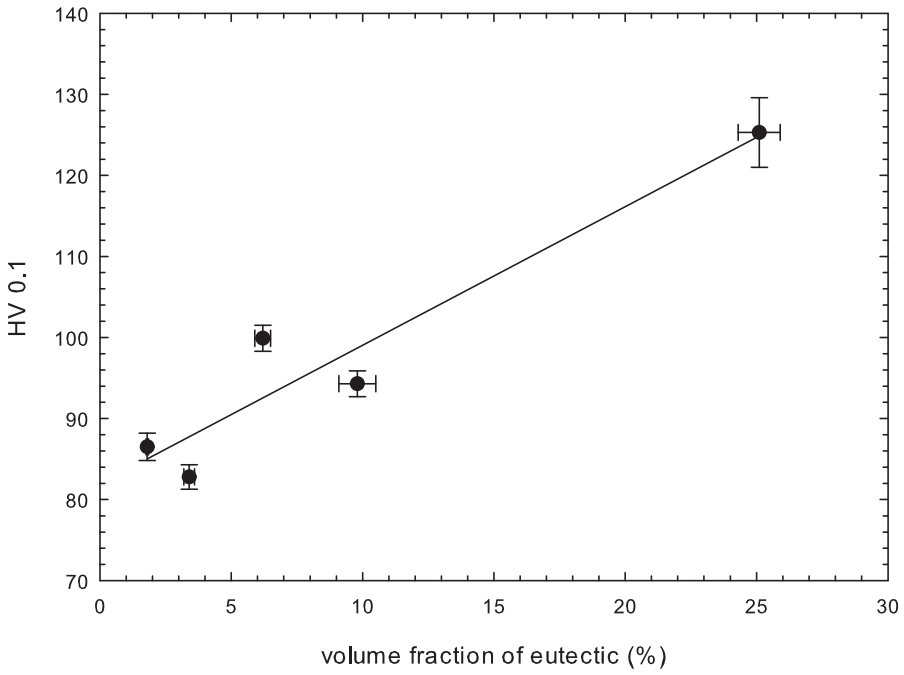

Figure 5.5: Correlation of the Vickers hardness with the volume fraction of eutectic.

6. Conclusions

As-cast samples of Mg6Zn alloy were subjected to isochronal annealing with steps 20 °C / 20 min. Measurements of mechanical properties and defect studies were performed after each annealing step. Precipitation hardening and presence of misfit open-volume defects introduced by formation of Zn-rich precipitates were observed at the temperature range 210–250 °C.

Samples of WE43 alloy and WE43 alloy modified by addition of 14 wt.% and 26 wt.% of zinc were investigated. Icosahedral phase $Mg_3Zn_6Y_1$ was identified in the samples of WE43+14Zn and WE43+26Zn alloys by X-ray diffraction measurements. It was found that positron trapping at vacancy-like defects associated with interface between the icosahedral phase $Mg_3Zn_6Y_1$ and Mg matrix occurs in the WE43+14Zn and WE43+26Zn alloys.

Investigations of MgZnAl-based alloys were performed as well. Presence of icosahedral $Mg_{44}Zn_{41}Al_{15}$ phase in the samples was confirmed by X-ray diffraction measurements. Vacancy-like defects were not observed in MgZnAl-based alloys by positron lifetime measurements. However, coincidence spectroscopy of Doppler broadening of annihilation radiation revealed that positron trapping in the vincinity of icosahedral $Mg_{44}Zn_{41}Al_{15}$ phase occurs. Hence in MgZnAl-based alloys certain fraction of positrons annihilate in the icosahedral phase but not trapped at vacancy-like defects.

Several hypotheses explaining different nature of positron trapping in WE43-based and MgZnAl-based alloys were proposed.

References

[1] Brandt W.: In: *Proceedings of the International School of Physics "Enrico Fermi"*, Course LXXXIII. Ed. W. Brandt, A. Dupasquier, North-Holland Publishing Company, Varenna (1983), 1.

[2] Brandt W., Paulin R.: *Positron implantation-profile effects in solids*, Phys. Rev. B **15** (1977), 2511–2518.

[3] Bergersen B., Pajanne E., Kubica P., Stott M. J., Hodges C. D.: *Positron diffusion in metals*, Solid State Commun. **15** (1974), 1377–1380.

[4] Puska M. J., Nieminen R. M.: *Theory of positrons in solids and on solid surfaces*, rev. Mod. Phys. **66** (1994), 841–897.

[5] Shechtman D., Blech I., Gratias D., Cahn, J.: *Metallic Phase with Long-Range Orientational Order and No Translational Symmetry*, Physical Review Letters **53** (1984), 1951.

[6] Landau L. D., Lifshitz E. M.: *Statisticheskaya Fizika (Statistical Physics) Pt. 1*, Nauka, Moscow (1976), 440. (Translated into English (Pergamon Press, Oxford 1980))

[7] Mihalkovič M., Zhu W.-J., Henley C. L., Oxborrow M.: *Icosahedral quasicrystal decoration models. I. Geometrical principles*, Phys. Rev. B **53** (1996), 9002.

[8] Vekilov Y. K., Chernikov M. A.: *Quasicrystals*, Phys.-Usp. **53** (2010) 537.

[9] Tsai A. P., Inoue A., Masumoto T.: *A Stable Quasicrystal in Al-Cu-Fe System*, Jpn. J. Appl. Phys. **26** (1987), L1505.

[10] Sastry G. V. S., Ramachandrarao P.: *A study of the icosahedral phase: $Mg_{32}(Al,Zn)_{49}$*, J. Mater. Res. **1** (1986), 247.

[11] Ohashi W., Spaepen F.: *Stable Ga–Mg–Zn quasi-periodic crystals with pentagonal dodecahedral solidification morphology*, Nature **330** (1987), 555.

[12] Yi S., Park E. S., Ok J. B., Kim W. T., Kim D. H.: *(Icosahedral phase + α-Mg) two phase microstructures in the Mg-Zn-Y ternary system*, Materials Science and Engineering A **300** (2001), 312–315.

[13] In Wikipedia: *Penrose tiling*, http://en.wikipedia.org/wiki/Penrose_tiling (2011).

[14] Meyers M. A., Chawla K. K.: *Mechanical Behavior of Materials (Second edition)*, Cambridge University Press, Cambridge (2009), 221.

[15] Bečvář F., Čížek J., Procházka I., Janotová J.: *The asset of ultra-fast digitizers for positron-lifetime spectroscopy*, Nucl. Instr. Meth. A **539** (2005), 372.

[16] Bečvář F., Čížek J., Procházka I.: *High-resolution positron lifetime measurement using ultra fast digitizers Acqiris DC211*, Applied Surface Science **255** (2008), 111–114.

[17] Bečvář F.: *Methodology of positron lifetime spectroscopy: Present status and perspectives*, Nucl. Instr. Meth. B **261** (2007), 871–874.

[18] Clark J.B., Zabdyr L., Moser Z.: *Phase diagram of Binary Magnesium Alloys*, ASM International (1988) 353–364.

[19] Chadwick R. J.: *The constitution of the Alloys of Magnesium and Zinc*, J. Inst. Met. **39** (1928), 285–299.

[20] Hume-Rothery W., Rounswfell E. D.: *The System Magnesium-Zinc*, J. Inst. Met. **41** (1929), 119–138.

[21] Clark J. B., Rhines F. N.: *Central Region of the Magnesium-Zinc Phase Diagram*, AIME **209** (1957), 425–430.

[22] Park J. J., Wyman L. L.: *Phase Relationships in Magnesium Alloys*, WADC Tech. Rept. 57-504, Astia Document No. AD142110 (1957), 1–27.

[23] Čížek J., Procházka I., Smola B., Stulíková I., Očenášek V.: *Influence of deformation on precipitation process in Mg–15 wt.% Gd alloy*, Journal of Alloys and Compounds **430** (2007), 92–96.

[24] Hautojärvi P., Corbel C.: In: *Proceedings of the International School of Physics "Enrico Fermi"*, Course CXXV, Ed. A. Dupasquier, A. P. Mills, IOS Press, Varenna (1995), 491–532.

[25] Smedskjaer L. C., Manninen M., Fluss M. J.: *An alternative interpretation of positron annihilation in dislocations*, J. Phys. F: Met. Phys. **10** (1980), 2237.

[26] Smola B.: *unpublished results*, (2011).

[27] Lee J. Y., Kim D. H., Lim H. K., Kim D. H.: *Effects of Zn / Y ratio on microstructure and mechanical properties of Mg-Zn-Y alloys*, Materials Letters **59** (2005), 3801–3805.

[28] Sato K., Murakami H., Kanazawa I., Kobayashi Y.: *Positron annihilation spectroscopy in the study of quasicrystals and their related materials*, Phys. Stat. Sol. C **4** (2007), 3455–3460.

List of Tables

List of Abbreviations

2D - Two-dimensional
3D - Three-dimensional
ADC - Analog-to-digital converter
BCC - Body-centered cubic
CDB - Coincidence Doppler broadening
CFD - Constant fraction discriminator
CFDD - Constant fraction differential discriminator
FCC - Face-centered cubic
FFA - Fast filtering amplifier
HV - Vickers pyramind number
IT - Inverting transformer
LT - Lifetime spectroscopy
PMT - Photomultiplier
SA - Spectroscopic amplifier
SAED - Selected area electron diffraction
SCA - Single channel analyzer
SEM - Scanning electron microscopy
STM - Simple trapping model
TAC - Time-amplitude converter
XRD - X-ray diffraction